J. Fluid Mech. (2007), *vol.* 581, *pp.* 167–197.
doi:10.1017/S0022112007005654 Printed in the United Kingdom

Structural sensitivity of the first instability of the cylinder wake

FLAVIO GIANNETTI AND PAOLO LUCHINI
DIMEC, Università di Salerno, Via Ponte don Melillo, 84084 Fisciano (SA), Italy

(Received 18 May 2004 and in revised form 11 December 2006)

The stability properties of the flow past an infinitely long circular cylinder are studied in the context of linear theory. An immersed-boundary technique is used to represent the cylinder surface on a Cartesian mesh. The characteristics of both direct and adjoint perturbation modes are studied and the regions of the flow more sensitive to momentum forcing and mass injection are identified. The analysis shows that the maximum of the perturbation envelope amplitude is reached far downstream of the separation bubble, where as the highest receptivity is attained in the near wake of the cylinder, close to the body surface. The large difference between the spatial structure of the two-dimensional direct and adjoint modes suggests that the instability mechanism cannot be identified from the study of either eigenfunctions separately. For this reason a structural stability analysis of the problem is used to analyse the process which gives rise to the self-sustained mode. In particular, the region of maximum coupling among the velocity components is localized by inspecting the spatial distribution of the product between the direct and adjoint modes. Results show that the instability mechanism is located in two lobes placed symmetrically across the separation bubble, confirming the qualitative results obtained through a locally plane-wave analysis. The relevance of this novel technique to the development of effective control strategies for vortex shedding behind bluff bodies is illustrated by comparing the theoretical predictions based on the structural perturbation analysis with the experimental data of Strykowski & Sreenivasan (*J. Fluid Mech.* vol. 218, 1990, p. 71).

1. Introduction

Spatially developing flows such as mixing layers, wakes and jets, may sustain in specific parameter ranges, synchronized periodic oscillations over extended regions of the flow field, displaying there an intrinsic dynamics characterized by a sharp frequency selection. Under these conditions, the whole flow field behaves like a global oscillator and the structure underlying the spatial distribution of the fluctuations is usually termed 'global mode'. The spatio-temporal evolution of such flows has been clarified considerably only in recent years: progress was made through model equations, experiments, stability analysis and direct numerical simulations. A theoretical approach to this class of problems was formulated by Chomaz, Huerre & Redekopp (1991), Monkewitz, Huerre & Chomaz (1993) and Le Dizs *et al.* (1996) in the context of flows with properties slowly varying in space. Relying only on a local analysis, they were able to show that such flows may exhibit internal resonance when a region of absolute instability (Briggs 1964; Bers 1975; Huerre & Monkewitz 1985, 1990) of sufficient size develops. The resonance is self-excited and is characterized by a well-defined frequency. The important link between the global and local instability properties, both in the linear and fully nonlinear regime, is obtained via a WKBJ

approach (Bender & Orszag 1978; Hinch 1994): the theory identifies a specific spatial position in the absolutely unstable region which acts as a 'wavemaker', providing a precise frequency selection criterion and revealing some important insights pertaining to the forcing of these modes. In particular, in a linear setting, the complex global frequency ω_g is obtained by the saddle-point condition,

$$\omega_g = \omega_0(X_s) \quad \text{with} \quad \frac{\partial \omega_0}{\partial X}(X_s) = 0, \tag{1.1}$$

based on the analytic continuation of the local absolute frequency curve $\omega_0(X)$ in the complex X-plane, with X denoting here the slow streamwise variable. Although this asymptotic theory yields accurate predictions for slowly evolving flows, in many real configurations the assumptions underlying the WKBJ approach are not met very closely. This is the case of bluff-body wakes, where strong non-parallel effects prevent us from using asymptotic theory. In such cases, a numerical modal analysis must be used to determine the characteristics of the instability and to find its critical Reynolds number. One of the most common examples is given by the flow around an infinitely long circular cylinder. This type of configuration has been investigated for a long time and accurate experimental data are now available to test the theoretical predictions. The steady two-dimensional symmetric flow existing around the cylinder at low Reynolds numbers becomes unstable when Re is increased beyond the critical value $Re_c \approx 47$ (Provansal, Mathis & Boyer 1987). The transition from the steady to the unsteady state occurs via a Hopf bifurcation (Provansal, Mathis & Boyer 1987; Sreenivasan, Strykowski & Olinger 1987; Noack & Eckelmann 1994) which breaks the symmetry of the flow field and gives rise to a periodic self-sustained structure usually termed the von Kármán vortex street. For Reynolds numbers lower than $Re_{c,2}$, where $180 \lesssim Re_{c,2} \lesssim 190$, the flow remains strictly two-dimensional (Williamson 1988, 1996; Karniadakis & Triantafyllou 1992; Barkley & Henderson 1996) so that the occurrence of the first instability can be predicted through a two-dimensional analysis.

In recent years, direct numerical simulations have been repeatedly used to study the development of the von Kármán vortex street and to locate the onset of the instability. Solving the full nonlinear temporal problem, however, is not the only way to predict the bifurcation point. An alternative approach, which can unveil many of the features of the global mode dynamics, consists in using linear theory: in this approach, the growth of the instability is predicted by solving a two-dimensional generalized eigenvalue problem derived from a discretization of the linearized Navier–Stokes equations. The large memory requirements necessary for the implementation of this method have drastically limited its use in the past. Examples can be found in Winters, Cliffe & Jackson (1986) and Jackson (1987), who determined the critical Reynolds number and the vortex shedding frequency by solving an extended set of time-independent equations generated by a finite-element procedure. Zebib (1987) and Hill (1992) located the critical point, evaluating both the base flow and the eigenvalues with a more accurate spectral technique. The large memory capabilities of modern computers have renewed the interest in this approach, which can now be used to tackle more complex flow configurations. In this paper, a global analysis of the flow around a circular cylinder is performed using an immersed-boundary technique. The properties of the adjoint eigenfunctions are here used in a novel way to locate the core of the instability and to verify the predictions based on asymptotic theory. Results obtained with the latter approach are used for comparison. Finally, the new technique is used to perform an analysis of the eigenvalue sensitivity to structural perturbations of the governing equations and the results are compared with the numerical and experimental data of Strykowski & Sreenivasan (1990).

2. Problem formulation

We investigate the stability characteristics of the two-dimensional flow arising around an infinitely long circular cylinder invested by a uniform stream. A Cartesian coordinate system is placed in the cylinder centre, with the x-axis pointing in the flow direction and the z-axis running along the cylinder centreline. For $Re < Re_{2,c}$, the fluid motion can be described by the two-dimensional unsteady incompressible Navier–Stokes equations

$$\frac{\partial \boldsymbol{U}}{\partial t} + \boldsymbol{U}\cdot\nabla\boldsymbol{U} = -\nabla P + \frac{1}{Re}\Delta\boldsymbol{U}, \tag{2.1a}$$

$$\nabla\cdot\boldsymbol{U} = 0, \tag{2.1b}$$

where $\boldsymbol{U}$ is the velocity vector with components $\boldsymbol{U} = (U, V)$ and P is the reduced pressure. Equations (2.1) are made dimensionless using the cylinder diameter D^* as the characteristic length scale, the velocity of the incoming uniform stream U^*_∞ as the reference velocity and $\rho^* U^{*2}_\infty$ as the reference pressure. Thus,

$$Re = \frac{U^*_\infty D^*}{\nu^*} \tag{2.2}$$

is the Reynolds number based on the cylinder diameter. Equations (2.1) are supplemented by the usual boundary conditions. In particular, on the surface of the cylinder Γ_c the no-slip and no-penetration conditions require both velocity components to vanish,

$$\boldsymbol{U} = \boldsymbol{0} \qquad \text{on} \quad \Gamma_c, \tag{2.3}$$

while in the far field the flow approaches the incoming uniform stream asymptotically:

$$\boldsymbol{U} \to U_\infty \boldsymbol{i} \qquad \text{as } x^2 + y^2 \to \infty. \tag{2.4}$$

The indeterminacy of the pressure field is removed by specifying the value of p at a given point of the domain. Here and in the following, the symbols $\boldsymbol{i}$ and $\boldsymbol{j}$ are used to indicate the unit vectors of the Cartesian system of coordinate, while $\| \ \|$ and $| \ |$ denote, respectively, the Euclidean norm of a vector and the modulus of a complex number.

2.1. *Linear stability*

The onset of the instability is studied in linear theory by using a normal-mode analysis. The total field $\boldsymbol{Q} = \{\boldsymbol{U}, P\}$ is decomposed into the sum of a steady part and a small unsteady perturbation as

$$\boldsymbol{U}(x, y, t) = \boldsymbol{U}_b(x, y) + \epsilon\ \boldsymbol{u}(x, y, t), \tag{2.5a}$$

$$P(x, y, t) = P_b(x, y) + \epsilon\ p(x, y, t), \tag{2.5b}$$

where the amplitude ϵ is assumed small. Introducing (2.5) into (2.1) and linearizing, we obtain two problems describing the spatial structure of the base flow and the evolution of the unsteady perturbation. In particular, the base flow is governed by the steady version of (2.1), whereas the perturbed field is described by the following set of linearized unsteady Navier–Stokes equations (LNSE)

$$\frac{\partial \boldsymbol{u}}{\partial t} + \boldsymbol{L}\{\boldsymbol{U}_b, Re\}\boldsymbol{u} = -\nabla p + \boldsymbol{f} \tag{2.6a}$$

$$\nabla\cdot\boldsymbol{u} = m. \tag{2.6b}$$

In the above equations, $\boldsymbol{L}$ stands for the linearized Navier–Stokes operator which in vector notation can be written as

$$\boldsymbol{L}\{\boldsymbol{U}_b, Re\}\boldsymbol{u} = \boldsymbol{U}_b \cdot \nabla \boldsymbol{u} + \boldsymbol{u} \cdot \nabla \boldsymbol{U}_b - \frac{1}{Re}\Delta \boldsymbol{u}, \tag{2.7}$$

while the source terms $\boldsymbol{f} = \{f_x, f_y\}$ and m have been introduced to account for a possible physical forcing mechanism. In this paper, we will assume that both the forcing and the initial conditions used to solve problem (2.6) have compact support so that all the components of the perturbation $\boldsymbol{q} = \{\boldsymbol{u}, p\}$ vanish as $r = (x^2 + y^2)^{1/2}$ tends to infinity. Thus, the appropriate conditions used to solve the differential problem (2.6) can be stated as

$$\boldsymbol{u}(x, y, t) = \boldsymbol{u}_w(x, y, t) \quad \text{on} \quad \Gamma_c \quad \forall t, \tag{2.8a}$$

$$\boldsymbol{q}(x, y, t) \to \boldsymbol{0} \quad \text{as} \quad r \to \infty \quad \forall t, \tag{2.8b}$$

$$\boldsymbol{u}(x, y, t) = \boldsymbol{u}_{in}(x, y) \quad \text{for} \quad t = 0, \tag{2.8c}$$

where we have denoted with $\boldsymbol{u}_{in}(x, y)$ the initial condition and with $\boldsymbol{u}_w(x, y, t)$ the value assumed by the solution on the cylinder surface Γ_c. In particular, in this paper, we are interested in the global modes of the linearized Navier–Stokes equations, i.e. non-trivial solutions of (2.6) of the form

$$\boldsymbol{u}(x, y, t) = \hat{\boldsymbol{u}}(x, y)\exp(\sigma t), \tag{2.9a}$$

$$p(x, y, t) = \hat{p}(x, y)\exp(\sigma t). \tag{2.9b}$$

Here, σ is a complex number while the complex field $\hat{\boldsymbol{q}} = \{\hat{\boldsymbol{u}}, \hat{p}\}$ satisfies the homogeneous equations

$$\sigma \hat{\boldsymbol{u}} + \boldsymbol{L}\{\boldsymbol{U}_b, Re\}\hat{\boldsymbol{u}} + \nabla \hat{p} = \boldsymbol{0}, \tag{2.10a}$$

$$\nabla \cdot \hat{\boldsymbol{u}} = 0, \tag{2.10b}$$

along with homogeneous boundary conditions on the cylinder surface

$$\hat{\boldsymbol{u}} = \boldsymbol{0} \qquad \text{on} \quad \Gamma_c \tag{2.11}$$

and appropriate far-field radiation conditions. This means that far enough from the cylinder, the perturbation behaves locally as an outgoing plane wave. While this last requirement enforces the correct causality relation, it does not generally imply that the disturbance vanishes at infinity. For the cylinder case, however, the spreading of the wake with the resulting attenuation of the vorticity and the rapid decay of the outer potential field produce a reduction of the perturbation amplitude with the radial distance. Thus, in our case, the far-field conditions may be formulated as

$$\hat{\boldsymbol{q}} = \{\hat{\boldsymbol{u}}, \hat{p}\} \to \{\boldsymbol{0}, 0\} \qquad \text{as} \quad r \to \infty. \tag{2.12}$$

The system of equations (2.10) along with the boundary conditions (2.11) and (2.12) gives rise to a generalized eigenvalue problem for the complex frequency σ. For $\mathrm{Re}(\sigma) < 0$ the flow is stable while for $\mathrm{Re}(\sigma) > 0$ the mode is unstable and the perturbation grows exponentially in time until nonlinear effects become important.

2.2. *Adjoint equations*

The adjoint of a linear operator is indeed one of the most important and useful concepts in functional analysis. Its application to the solution of differential equations is strictly related to the use of Green's functions and traces back to the original work of Lagrange in the eighteenth century. In fluid mechanics, it has been largely used to tackle problems in receptivity, transition, turbulence control and meteorology. The

adjoint linearized Navier–Stokes operator is defined using the generalized Lagrange identity (Ince 1926). For any pair of suitably differentiable fields $\boldsymbol{q} \equiv \{\boldsymbol{u}, p\}$ and $\boldsymbol{g}^+ \equiv \{\boldsymbol{f}^+, m^+\}$, which need not satisfy equations (2.6), the following Lagrange identity is constructed using differentiation by parts

$$\left[\left(\frac{\partial \boldsymbol{u}}{\partial t} + \boldsymbol{L}\{\boldsymbol{U}_b, Re\}\boldsymbol{u} + \nabla p\right)\cdot \boldsymbol{f}^+ + \nabla\cdot \boldsymbol{u}\hat{m}^+\right] + \left[\boldsymbol{u}\cdot\left(\frac{\partial \boldsymbol{f}^+}{\partial t} + \boldsymbol{L}^+\{\boldsymbol{U}_b, Re\}\boldsymbol{f}^+ + \nabla m^+\right) + p\ \nabla\cdot \boldsymbol{f}^+\right] = \frac{\partial \boldsymbol{u}\cdot \boldsymbol{f}^+}{\partial t} + \nabla\cdot \boldsymbol{J}(\boldsymbol{q}, \boldsymbol{g}^+). \quad (2.13)$$

In (2.13), $\boldsymbol{J}(\boldsymbol{q}, \boldsymbol{g}^+)$ is the 'bilinear concomitant'

$$\boldsymbol{J}(\boldsymbol{q}, \boldsymbol{g}^+) = \boldsymbol{U}_b(\boldsymbol{u}\cdot \boldsymbol{f}^+) + \frac{1}{Re}(\nabla \boldsymbol{f}^+\cdot \boldsymbol{u} - \nabla \boldsymbol{u}\cdot \boldsymbol{f}^+) + m^+\ \boldsymbol{u} + p\boldsymbol{f}^+ \quad (2.14)$$

and $\boldsymbol{L}^+$ is the adjoint linearized Navier–Stokes operator which in vector notation can be expressed as

$$\boldsymbol{L}^+\{\boldsymbol{U}_b, Re\}\boldsymbol{f}^+ = \boldsymbol{U}_b\cdot \nabla \boldsymbol{f}^+ - \nabla \boldsymbol{U}_b\cdot \boldsymbol{f}^+ + \frac{1}{Re}\Delta \boldsymbol{f}^+. \quad (2.15)$$

Integration of (2.13) over space and time and use of the divergence theorem gives the generalized Green's theorem (Morse & Feshbach 1953) for the LNSE. Examining the second term in the square brackets on the left-hand side of the Lagrange identity (2.13), we define the adjoint equations as

$$\frac{\partial \boldsymbol{f}^+}{\partial t} + \boldsymbol{L}^+\{\boldsymbol{U}_b, Re\}\boldsymbol{f}^+ + \nabla m^+ = \boldsymbol{0}, \quad (2.16a)$$

$$\nabla\cdot \boldsymbol{f}^+ = 0. \quad (2.16b)$$

It is judicious manipulation of the right-hand side of (2.13) that engenders the usefulness of the adjoint solutions $\boldsymbol{g}^+$. In this paper, we are mainly interested in the adjoint modes, i.e. non-trivial solutions of the adjoint linearized Navier–Stokes equations (2.16) of the form

$$\boldsymbol{f}^+(x, y, t) = \hat{\boldsymbol{f}}^+(x, y)\exp(-\sigma t), \quad (2.17a)$$

$$m^+(x, y, t) = \hat{m}^+(x, y)\exp(-\sigma t). \quad (2.17b)$$

More specifically, if $\boldsymbol{q}(x, y, t) = \hat{\boldsymbol{q}}(x, y)\exp(\sigma t)$ is a global mode of the LNSE corresponding to the eigenvalue σ, we define $\boldsymbol{g}^+(x, y, t) = \hat{\boldsymbol{g}}^+(x, y)\exp(-\sigma t)$ its adjoint global mode if the complex field $\hat{\boldsymbol{g}}^+ = \{\hat{\boldsymbol{f}}^+, \hat{m}^+\}$ is a non-trivial solution of equations

$$-\sigma \hat{\boldsymbol{f}}^+ + \boldsymbol{L}^+\{\boldsymbol{U}_b, Re\}\hat{\boldsymbol{f}}^+ + \nabla \hat{m}^+ = \boldsymbol{0}, \quad (2.18a)$$

$$\nabla\cdot \hat{\boldsymbol{f}}^+ = 0, \quad (2.18b)$$

satisfying homogeneous boundary conditions on the cylinder surface

$$\hat{\boldsymbol{f}}^+(x, y) = \boldsymbol{0} \quad \text{on} \quad \Gamma_c \quad (2.19)$$

and appropriate radiation conditions in the far field. As for the direct mode, this does not generally mean that the adjoint field has to vanish as the radial distance $r \to \infty$. However, in our case, the particular structure of the base flow leads to a rapid decay of the adjoint mode, so that the far-field conditions become

$$\hat{\boldsymbol{g}}^+ = \{\hat{\boldsymbol{f}}^+, \hat{m}^+\} \to \boldsymbol{0} \quad \text{as} \quad r \to \infty. \quad (2.20)$$

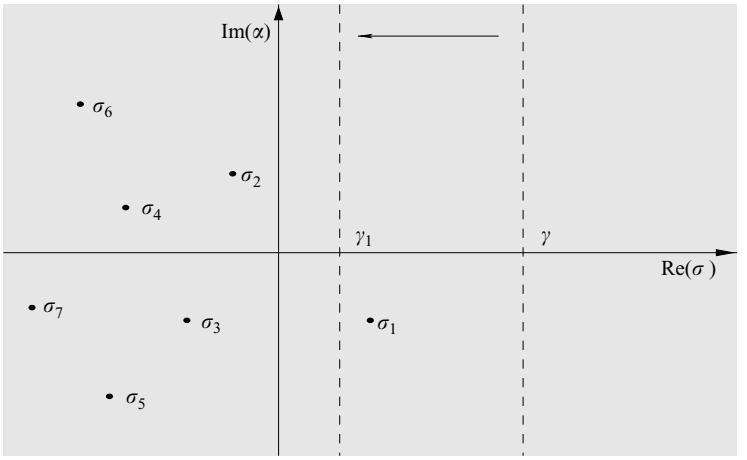

FIGURE 1. Schematic picture representing the Bromwich integration path and the poles in the complex σ-plane.

3. Receptivity to initial conditions and external forcing

The adjoint equations can be used to evaluate the effects of generic initial conditions and forcing terms on the time-asymptotic behaviour of the solution of (2.6) and (2.8). A way of achieving this is to take a Laplace transform in time of (2.6) and solve for the transformed field $\hat{\boldsymbol{q}} = \{\hat{\boldsymbol{u}}, \hat{p}\}$. This is defined as

$$\hat{\boldsymbol{q}}(x, y, \sigma) = \int_0^{+\infty} \boldsymbol{q}(x, y, t)\exp(-\sigma t)\,\mathrm{d}t \tag{3.1}$$

and satisfies the inhomogeneous system of second-order partial differential equations

$$\sigma\hat{\boldsymbol{u}} + \boldsymbol{L}\{\boldsymbol{U}_b, Re\}\hat{\boldsymbol{u}} + \nabla\hat{p} = \hat{\boldsymbol{f}} + \boldsymbol{u}_{in}, \tag{3.2a}$$

$$\nabla\cdot\hat{\boldsymbol{u}} = \hat{m}, \tag{3.2b}$$

along with the boundary conditions

$$\hat{\boldsymbol{u}}(x, y, \sigma) = \hat{\boldsymbol{u}}_w(x, y, \sigma) \quad \text{on} \quad \Gamma_c, \tag{3.3a}$$

$$\hat{\boldsymbol{u}}(x, y, \sigma) \to \boldsymbol{0} \quad \text{as} \quad r \to \infty. \tag{3.3b}$$

In the previous formulae $\hat{\boldsymbol{f}}$ and $\hat{m}$ are the Laplace transforms of the forcing functions $\boldsymbol{f}(x, y, t)$ and $m(x, y, t)$, $\hat{\boldsymbol{u}}_w$ represents the Laplace transform of the boundary condition $\hat{\boldsymbol{u}}_w$, while $\boldsymbol{u}_{in}(x, y) = \boldsymbol{u}(x, y, t = 0)$ denotes the initial condition used to solve the time-dependent problem (2.6). Once the solution of (3.2) and (3.3) is available, we recover the physical variables in the time domain in terms of the Bromwich integral in the complex σ-plane as

$$\boldsymbol{q}(x, y, t) = \frac{1}{2\pi\mathrm{i}} \int_{\gamma-\mathrm{i}\infty}^{\gamma+\mathrm{i}\infty} \hat{\boldsymbol{q}}(x, y, \sigma)\exp(\sigma t)\,\mathrm{d}\sigma, \tag{3.4}$$

where γ is a sufficiently large real positive number such that all the singularities of $\hat{\boldsymbol{q}}(x, y, \sigma)$ are located to the left of the integration path (see figure 1). The time-asymptotic behaviour of (3.4) can be estimated by the residues theorem. Suppose there exists an unstable global mode with eigenvalue σ_1, i.e. a non-trivial solution $\hat{\boldsymbol{q}}_1$ of (2.10), (2.11), (2.12) with $\sigma = \sigma_1$. In such a case, the Laplace transform $\hat{\boldsymbol{q}}(x, y, \sigma)$

has a pole at $\sigma = \sigma_1$. Since the asymptotic uniform flow is stable, no branch points exist in the half-plane $\mathrm{Re}(\sigma) > 0$. As a consequence, we can deform the integration path by lowering the value of γ and use the residues theorem to rewrite the solution as

$$\boldsymbol{q}(x, y, t) = \mathscr{R}[\hat{\boldsymbol{q}}(x, y, \sigma)]_{\sigma=\sigma 1}\exp(\sigma_1 t) + \frac{1}{2\pi \mathrm{i}} \int_{\gamma_1 - \mathrm{i}\infty}^{\gamma_1 + \mathrm{i}\infty} \hat{\boldsymbol{q}}(x, y, \sigma)\exp(\sigma t)\, \mathrm{d}\sigma. \tag{3.5}$$

Here, $\mathscr{R}[\hat{\boldsymbol{q}}(\sigma)]_{\sigma=\sigma_1}$ denotes the residue of $\hat{\boldsymbol{q}}(x, y, \sigma)$ at $\sigma = \sigma_1$, while the integration path lies now to the left of the pole σ_1 $(0 < \gamma_1 < \mathrm{Re}(\sigma_1))$. By assumption, the first term on the right-hand side of (3.5) grows exponentially in time and characterizes the long-time behaviour of the solution. In order to study the effect of the forcing terms, initial and boundary conditions on the time-asymptotic response of the system, we first express the residue $\mathscr{R}[\hat{\boldsymbol{q}}(x, y, \sigma)]_{\sigma=\sigma_1}$ in terms of the eigenfunction $\hat{\boldsymbol{q}}_1 = \{\hat{\boldsymbol{u}}_1, \hat{p}_1\}$ of (2.10). More specifically, if $\sigma = \sigma_1$ is a simple pole for the Laplace-transformed field, then we have

$$\mathscr{R}[\hat{\boldsymbol{q}}(x, y, \sigma)]_{\sigma=\sigma_1} = \lim_{\sigma \to \sigma_1} (\sigma - \sigma_1)\hat{\boldsymbol{q}}(x, y, \sigma) = A_1 \hat{\boldsymbol{q}}_1(x, y, \sigma_1), \tag{3.6}$$

where A_1 represents the amplitude of the global mode. This amplitude depends on the specific forcing functions, initial and boundary conditions chosen to solve the forced problem (3.2). Its value can be determined by suitable application of the generalized Lagrange identity (2.13) to the fields

$$\boldsymbol{q}(x, y, t) = \hat{\boldsymbol{q}}(x, y, \sigma)\exp(\sigma t), \tag{3.7}$$

$$\boldsymbol{g}_1^+(x, y, t) = \hat{\boldsymbol{g}}_1^+(x, y, \sigma_1)\exp(-\sigma_1 t), \tag{3.8}$$

where $\hat{\boldsymbol{q}} = \{\hat{\boldsymbol{u}}, \hat{p}\}$ is the solution of the transformed equations (3.2), (3.3) and $\hat{\boldsymbol{g}}_1^+ = \{\hat{\boldsymbol{f}}_1^+, \hat{m}_1^+\}$ denotes the adjoint global mode corresponding to the eigenvalue σ_1. Applying the Lagrange identity, integrating over the flow domain $\mathscr{D}$ and using the boundary conditions and the divergence theorem we arrive at the identity:

$$\begin{aligned} &\int_{\mathscr{D}} (\sigma \hat{\boldsymbol{u}} + \boldsymbol{L}\{\boldsymbol{U}_b, Re\}\hat{\boldsymbol{u}} + \nabla \hat{p}) \cdot \hat{\boldsymbol{f}}_1^+ + \nabla \cdot \hat{\boldsymbol{u}}\ \hat{m}_1^+ \, \mathrm{d}S \\ &\quad + \int_{\mathscr{D}} \hat{\boldsymbol{u}} \cdot (-\sigma_1 \hat{\boldsymbol{f}}_1^+ + \boldsymbol{L}^+\{\boldsymbol{U}_b, Re\}\hat{\boldsymbol{f}}_1^+ + \nabla \hat{m}_1^+) + \hat{p} \nabla \cdot \hat{\boldsymbol{f}}_1^+ \, \mathrm{d}S \\ &= \int_{\mathscr{D}} (\sigma - \sigma_1)\hat{\boldsymbol{u}} \cdot \hat{\boldsymbol{f}}_1^+ \, \mathrm{d}S - \oint_{\Gamma_c} \boldsymbol{J}(\hat{\boldsymbol{q}}, \hat{\boldsymbol{g}}_1^+) \cdot \boldsymbol{n} \, \mathrm{d}l, \end{aligned} \tag{3.9}$$

relating the transformed variables and the adjoint global mode. Here, $\boldsymbol{n}$ denotes the cylinder's normal, while $\mathrm{d}S$ and $\mathrm{d}l$ stand, respectively, for the surface differential and the arclength differential. Recalling now equations (2.18), (3.2) and (3.6) and taking the limit as $\sigma \to \sigma_1$, we obtain:

$$A_1 = \frac{\displaystyle\int_{\mathscr{D}} \hat{\boldsymbol{f}}_1^+ \cdot [\boldsymbol{u}_{in} + \hat{\boldsymbol{f}}] + \hat{m}_1^+ \hat{m} \mathrm{d}S + \oint_{\Gamma_c} \left[\frac{1}{Re} \nabla \hat{\boldsymbol{f}}_1^+ \cdot \hat{\boldsymbol{u}}_w + \hat{m}_1^+ \hat{\boldsymbol{u}}_w \right] \cdot \boldsymbol{n} \, \mathrm{d}l}{\displaystyle\int_{\mathscr{D}} \hat{\boldsymbol{f}}_1^+ \cdot \hat{\boldsymbol{u}}_1 \, \mathrm{d}S} \tag{3.10}$$

expressing the dependence of the global mode amplitude from the forcing functions, boundary and initial conditions. Because of linearity, the effects of each term in the numerator can be studied separately once the direct and adjoint eigenfunctions are determined numerically and a suitable normalization for both is chosen.

In particular, if the forcing functions or the initial conditions are localized in space (i.e. have a delta function form) the amplitude of the resulting mode is easily determined from the knowledge of the local values of $\boldsymbol{f}^+(x, y)$ and $m^+(x, y)$. In this sense, the adjoint field represents the Green's function for the receptivity problem.

4. Numerical approach

Several numerical techniques are available to solve the incompressible Navier–Stokes equations efficiently, each having advantages and drawbacks. The simple geometry treated in this paper makes the problem particularly suitable for the use of spectral techniques in cylindrical coordinates. Examples can be found in Zebib (1987), Yang & Zebib (1988), Hill (1992), Mittal & Balachandar (1996). More complex spectral and finite-element formulations were successively used by Noack & Eckelmann (1994), Barkley & Henderson (1996) and Blackburn & Henderson (1999) to study the three-dimensional stability of the cylinder wake and the two-dimensional vortex patterns generated by an oscillating cylinder. Another possible approach, which is often used to treat problems with complex geometries and moving boundaries, is given by the immersed-boundary technique. In this latter method, the equations are discretized using finite differences on a simple orthogonal mesh (in most cases Cartesian) whose nodes do not necessarily coincide with the body surface. The boundary conditions are then imposed by using an appropriate interpolation which preserves the order of accuracy of the numerical scheme.

In a preliminary stage of this study, the stability of the flow field was investigated by using cylindrical coordinates and a mixed spectral finite-difference approach. The velocity components were expanded in Fourier modes, while the radial derivatives were approximated by standard second-order finite differences. With this scheme we were able to re-obtain most of the results found in the literature. The computations, however, showed that near the critical Reynolds number the maximum of the eigenfunction is attained far behind the cylinder surface, in a region which extends beyond the computational domain used by Zebib (1987) and Hill (1992). This was unexpected since both of them obtained converged results for the eigenvalues. In order to explain this behaviour we decided to investigate the far-field spatial structure of the direct and adjoint modes. Cylindrical coordinates, however, are not very suitable for this purpose since their use involves a rapid degradation of the azimuthal resolution with radial distance. As a consequence, a large number of Fourier modes (too large for our computational facilities) were required to accurately resolve the details of the flow in the far wake. The immersed-boundary technique, on the other hand, is more appropriate treating this kind of problem since with this approach we can achieve a better resolution of the wake region with substantial memory savings. Furthermore, the use of a rectangular Cartesian mesh allows an easier treatment of the outflow numerical boundary conditions, while the effects of different body geometries on the stability of the flow can easily be accounted for with little extra effort. Considering all these issues, we decided to tackle the problem using this last approach.

4.1. *Immersed boundary*

The steady version of (2.1) and the linearized equations (2.10), both written in conservative form, are discretized with second-order finite-differences over a staggered Cartesian mesh. In order to resolve the details of the flow in the near wake better, Roberts stretching transformations (Tannehil, Anderson & Pletcher 1997, pp. 336–337) are used to cluster the mesh points smoothly near the cylinder centre (x_c, y_c). In particular, the coordinates (x_i, y_j) of a node in the computational mesh are obtained

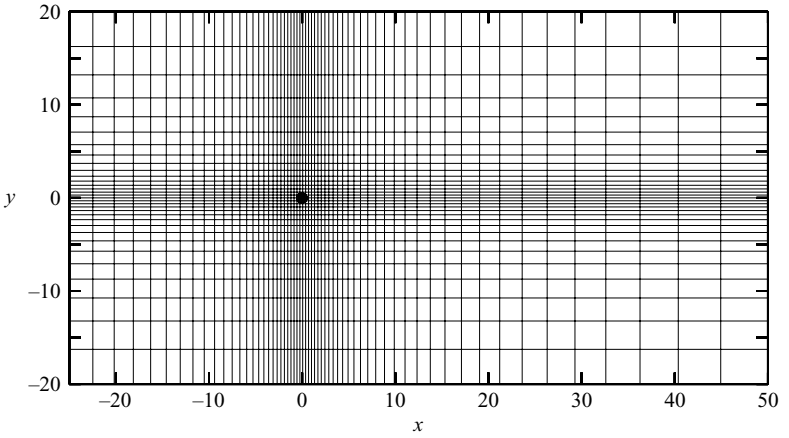

FIGURE 2. An example of a mesh grid used for computations. Only one out of ten lines passing through the pressure nodes is drawn to make the graph clearer ($\tau_x = 6.4$, $\tau_y = 6.8$, $Lx = 75$, $Ly = 40$).

by evaluating the following expressions

$$x_i = x_c\left\{1 + \frac{\sinh\left[\tau_x(i/n_x - B_x)\right]}{\sinh\left(\tau_x B_x\right)}\right\}, \qquad y_j = y_c\left\{1 + \frac{\sinh\left[\tau_y(i/n_y - B_y)\right]}{\sinh\left(\tau_y B_y\right)}\right\} \tag{4.1}$$

where i and j are the grid indexes and B_x and B_y are coefficients given by

$$B_x = \frac{1}{2\tau_x}\ln\left[\frac{1 + (\exp(\tau_x) - 1)(x_c/L_x)}{1 + (\exp(-\tau_x) - 1)(x_c/L_x)}\right], \quad B_y = \frac{1}{2\tau_y}\ln\left[\frac{1 + (\exp(\tau_y) - 1)(y_c/L_y)}{1 + (\exp(-\tau_y) - 1)(y_c/L_y)}\right]. \tag{4.2}$$

In these formulae, L_x and L_y are the horizontal and vertical widths of the computational mesh, while n_x and n_y represent the number of points used in the x and y directions, respectively. The two stretching parameters τ_x and τ_y control the clustering of points and can range from zero (no stretching) to large values that produce the largest refinement near (x_c, y_c). After these transformations, a simple translation is performed to place the cylinder centre at (0, 0) exactly. As an example, figure 2 shows a typical mesh used in the computations: here only one out of every ten lines is drawn to make the graph more readable.

The presence of the cylinder is represented by an immersed-boundary technique similar to that used by Fadlun *et al.* (2000). Thus, the entire domain is covered by computational cells and there is no need for body-fitted coordinates. The boundary conditions on the surface of the cylinder Γ_c are imposed through a linear interpolation which preserves the second-order accuracy of the finite-difference scheme. Several interpolation procedures have been proposed in the past: in Fadlun *et al.* (2000), the velocity at the first grid point external to the body is obtained by linearly interpolating the velocity at the second grid point (which is instead obtained by directly solving the Navier–Stokes equations) and the velocity at the body surface; in their numerical algorithm this condition is approximately enforced by applying momentum forcing inside the flow field. The interpolation direction is either the streamwise or the transverse direction, but the choice between them is not specified. Mohd-Yusof (1997) used a more complex interpolation scheme which involved forcing the Navier–Stokes equations both inside and on the surface of the body. In particular, the no-slip conditions were imposed at

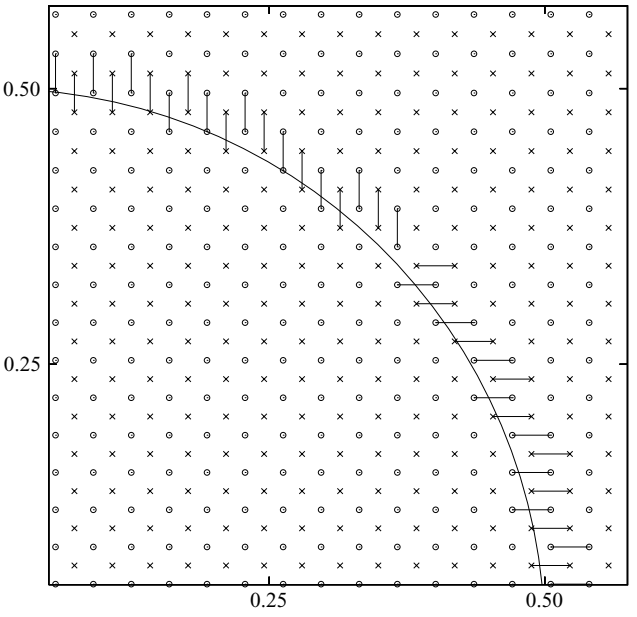

FIGURE 3. Example of immersed-boundary grid: ○, horizontal velocity component, u; ×, vertical velocity components v. Lines connect points involved in the interpolation.

the point of the boundary touched by the wall-normal line passing through the closest internal point, using bilinear interpolations for this purpose. Finally, Kim, Kim & Choi (2001) introduced a mass injection forcing to satisfy the continuity equation for the cells containing the immersed boundary. When the number of points used in the simulation is sufficient to represent the details of the body shape, all these schemes have similar performances, showing that the substantial increase in the code complexity owing to the use of sophisticated interpolation procedures is often not repaid by an adequate improvement of the numerical accuracy. We therefore decided to follow a slightly different but simpler approach. The interpolation was performed using the point closest to the body surface (which can be either an internal or an external point) and the following point on the exterior of the cylinder. The interpolation is performed either in the streamwise or transverse direction according to which one is closest to the local normal. An example of a grid used for the immersed-boundary technique and the nodes involved in the interpolation scheme are shown in figure 3.

On the external boundary of the rectangular computational domain Γ_{ext}, the conditions depicted in figure 4 are used to close the system of algebraic equations. In particular, for both the base flow and the perturbation, the values of the velocity components are imposed at the inlet boundary Γ_{in},

$$U = 1, \quad V = 0 \qquad \text{on } \Gamma_{in}, \tag{4.3a}$$

$$u = 0, \quad v = 0 \qquad \text{on } \Gamma_{in}, \tag{4.3b}$$

symmetry boundary conditions are enforced on the upper and lower boundaries Γ_{up} and Γ_{low}

$$\frac{\partial U}{\partial y} = 0, \quad V = 0 \qquad \text{on } \Gamma_{up} \cup \Gamma_{low}, \tag{4.4a}$$

$$\frac{\partial u}{\partial y} = 0, \quad v = 0 \qquad \text{on } \Gamma_{up} \cup \Gamma_{low}, \tag{4.4b}$$

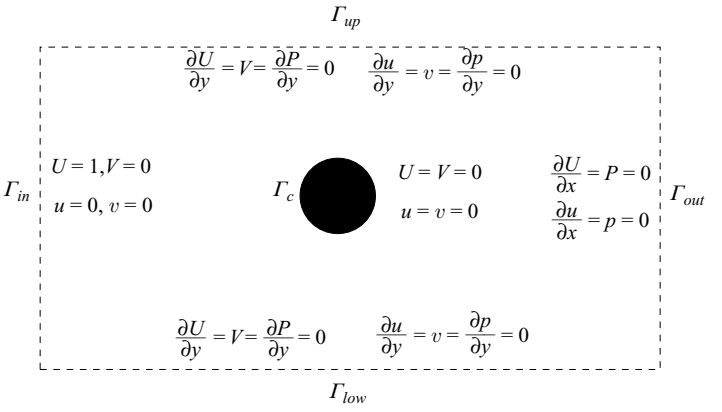

FIGURE 4. Computational domain and summary of the numerical boundary conditions used for the computations of the steady and unsteady linearized Navier–Stokes equations.

while the pressure and the streamwise derivative of the horizontal velocity components are set to zero on the outlet boundary Γ_{out}

$$\frac{\partial U}{\partial x} = 0, \quad P = 0 \qquad \text{on} \quad \Gamma_{out}, \tag{4.5a}$$

$$\frac{\partial u}{\partial x} = 0, \quad p = 0 \qquad \text{on} \quad \Gamma_{out}. \tag{4.5b}$$

These conditions enforce through the continuity equation a vanishing vertical velocity component on the outflow boundary. While for the base flow this requirement does not represent a problem, for the perturbation the application of such conditions results in unphysical oscillations of the solution in cases in which the global mode decays too slowly for the computational domain used. In order to allow more flexibility and obtain smoother fields, a second set of outflow boundary conditions has been implemented and tested. For both the perturbation and the base flow we impose on the outflow boundary

$$\frac{\partial V}{\partial x} = 0, \quad \frac{\partial P}{\partial x} = 0 \qquad \text{on} \quad \Gamma_{out}, \tag{4.6a}$$

$$\frac{\partial v}{\partial x} = 0, \quad \frac{\partial p}{\partial x} = 0 \qquad \text{on} \quad \Gamma_{out}, \tag{4.6b}$$

and prescribe the value of the pressure at a given point in the domain in order to remove its indeterminacy. Tests have shown that for the base flow, the differences in the solutions computed with (4.5*a*) and (4.6*a*) are negligible. The same conclusion is valid for the perturbation when the eigenfunction tail quickly decreases in the downstream direction. A benefit is instead achieved in cases in which the computational domain is not large enough and the global mode decays slowly. In those cases, conditions (4.6*b*) partially reduce the oscillations observed with (4.5) and produce smoother solutions. The differences in the computed eigenvalues are, however, always negligible. An explanation for such behaviour will be given in § 8, where a structural stability analysis for the flow around a circular cylinder is developed.

4.2. *Base flow*

The nonlinear system of algebraic equations deriving from the discretization of the nonlinear equations (2.1), along with their boundary conditions (4.3*a*), (4.4*a*) and (4.5*a*) (or (4.6*a*)), is solved by a Newton–Raphson procedure: at each step the linear

system

$$\boldsymbol{A}\left(Re, \boldsymbol{W}_b^{(n)}\right) \cdot \boldsymbol{w}_b^{(n)} = -\boldsymbol{rhs}^{(n)} \tag{4.7}$$

is inverted using a sparse LU decomposition and the base flow is then updated as

$$\boldsymbol{W}_b^{(n+1)} = \boldsymbol{W}_b^{(n)} + \boldsymbol{w}_b^{(n)}. \tag{4.8}$$

In this way all the equations of the system are treated simultaneously and the procedure is iterated until the elements of the residual vector $\boldsymbol{rhs}_b^{(n)}$ become smaller in magnitude than a given tolerance. In formula (4.7), $\boldsymbol{A}$ represents a large banded matrix obtained by the linearization of the original system of algebraic nonlinear equations, while $\boldsymbol{W}_b = \{(U_{i,j}, V_{i,j}, P_{i,j}) : 0 \leqslant i \leqslant n_x, 0 \leqslant j \leqslant n_y\}$ and $\boldsymbol{w}_b = \{(\Delta u_{i,j}, \Delta v_{i,j}, \Delta p_{i,j}) : 0 \leqslant i \leqslant n_x, 0 \leqslant j \leqslant n_y\}$ are vectors of triplets containing the values of the base flow components and their perturbation at different grid nodes, ordered in a lexicographic fashion.

4.3. *Eigenvalue solver and adjoint field*

Once the base flow is determined, the system of equations (2.10) is used to perform the stability analysis. After discretization, the equations and their boundary conditions (4.3*b*), (4.4*b*) and (4.5*b*) are recast in the form

$$[\boldsymbol{A}(Re, \boldsymbol{W}_b) + \sigma \boldsymbol{B}] \cdot \boldsymbol{w} = \boldsymbol{0}, \tag{4.9}$$

where $\boldsymbol{w} = \{(\hat{u}_{i,j}, \hat{v}_{i,j}, \hat{p}_{i,j}) : 0 \leqslant i \leqslant n_x, 0 \leqslant j \leqslant n_y\}$ is the right (or direct) eigenvector and $\boldsymbol{B}$ represents a diagonal matrix whose entries are 1 if the corresponding row contains the discretization of the horizontal or vertical component of the momentum equation, 0 otherwise. In order to study the receptivity of the dominant mode to the initial conditions and to the forcing terms, we must also compute the adjoint field $\hat{\boldsymbol{g}}^+$. This can be achieved in two different ways: a first possibility is to consider the discrete adjoint problem

$$\boldsymbol{\xi} \cdot [\boldsymbol{A}(Re, \boldsymbol{W}_b) + \sigma \boldsymbol{B}] = \boldsymbol{0}. \tag{4.10}$$

Here the computational vector $\boldsymbol{\xi} \equiv \{(\hat{f}_x^+(x_i, y_j), \hat{f}_y^+(x_i, y_j), \hat{m}^+(x_i, y_j)) : 0 \leqslant i \leqslant n_x, 0 \leqslant j \leqslant n_y\}$ is the left eigenvector of the discrete problem and, as can be easily deduced, it represents an approximation of the adjoint mode satisfying (2.18) and (2.19). Another possibility to evaluate numerically the adjoint field $\hat{\boldsymbol{g}}^+$ is to discretize directly the adjoint equations (2.18) and then determine the eigenvalues and the right eigenvectors of the resulting discrete problem. If the discretization is consistent, the two approaches, one based on the left eigenvectors of the discretized direct problem and one based on the right eigenvectors of the discretized adjoint problem, are equivalent and both solutions converge to the adjoint mode of the continuous differential equation. Here, we decided to rely on the first approach because it is easier to apply and automatically takes into account the correct boundary conditions for the adjoint field. The generalised eigenvalue problems (4.9) and (4.10) are solved numerically for σ by a variant of the classical inverse-iteration algorithm (see for example Golub & Van Loan 1989). If $\sigma^{(n)}$, $\boldsymbol{\xi}^{(n)}$ and $\boldsymbol{w}^{(n)}$ are, respectively, an approximation of the eigenvalue, left (adjoint) and right (direct) eigenvector of the discretized problem, a better estimate of these quantities is obtained by first evaluating

$$\boldsymbol{C}_n = \boldsymbol{A}(Re, \boldsymbol{W}_b) + \sigma^{(n)} \boldsymbol{B}, \tag{4.11}$$

$$\boldsymbol{w}^{(n+1)} = \boldsymbol{C}_n^{-1} \cdot \left(\boldsymbol{B} \cdot \boldsymbol{w}^{(n)}\right), \tag{4.12}$$

$$\boldsymbol{\xi}^{(n+1)} = \boldsymbol{\xi}^{(n)} \cdot \boldsymbol{B} \cdot \boldsymbol{C}_n^{-1}, \tag{4.13}$$

$$z^{(n+1)} = \boldsymbol{\xi}^{(n+1)} \cdot \boldsymbol{B}, \tag{4.14}$$

and then updating the eigenvalue as

$$\sigma^{(n+1)} = \sigma^{(n)} + \frac{\boldsymbol{z}^{(n+1)} \cdot \boldsymbol{w}^{(n)}}{\boldsymbol{z}^{(n+1)} \cdot \boldsymbol{w}^{(n+1)}}. \tag{4.15}$$

The whole procedure is iterated until $\Delta\sigma^{(n+1)} = |\sigma^{(n+1)} - \sigma^{(n)}|$ becomes smaller than a given tolerance. To avoid an unbounded growth of the solution, at each iteration step the resulting vectors are rescaled in a suitable manner. In this paper, for example, the right and left eigenvectors are normalized by requiring

$$\max_{x,y\in\mathscr{D}}\{|\hat{u}(x, y)|\} = 1, \qquad \int_{\mathscr{D}} \hat{\boldsymbol{f}}^{+} \cdot \hat{\boldsymbol{u}}\, \mathrm{d}S = 1. \tag{4.16}$$

From a practical point of view this is achieved by imposing at each iteration a discrete form of (4.16). The numerical procedure described above is obtained by simultaneously applying the classical inverse iteration algorithm to both the direct and adjoint problems (4.9) and (4.10). Instead of performing two separate computations, however, the right and left eigenvectors are updated simultaneously at each iteration: in this way the solution of the two problems proceeds in a coupled way and requires only a single LU decomposition for each step. In general, the convergence of the algorithm depends on the initial guesses used for the eigenvalue and the eigenvectors. Depending on the starting values, the numerical procedure described above may converge to the desired mode, to a different mode or even diverge. Our experience shows that if the value of $\sigma^{(0)}$ is chosen close enough to the eigenvalue of the desired mode, the algorithm converges quadratically to the correct solution independently from the guesses used for the eigenvectors.

The numerical vector $\boldsymbol{\xi}$ contains the components of the adjoint field at different grid locations and therefore it expresses the sensitivity of the unsteady flow to the forcing terms $\hat{\boldsymbol{f}}$ and $\hat{m}$ in (2.10). The components of the vector $\boldsymbol{z} \equiv (\boldsymbol{\xi} \cdot \boldsymbol{B}) = \{(\hat{u}_x^{+}(x_i, y_j), \hat{v}_y^{+}(x_i, y_j), \hat{p}^{+}(x_i, y_j)) : 0 \leqslant i \leqslant n_x, 0 \leqslant j \leqslant n_y\}$, on the other hand, measure the receptivity to the initial conditions used to march the unsteady linearised Navier–Stokes equations (2.6). This can be verified easily by discretizing in space the linearized equations of motion and then repeating for the semi-discrete equations the same steps as performed in § 3. As expected, the component $p^{+}(x_i, y_j)$ in $\boldsymbol{z}$ is identically zero, since the initial-value problem for the LNSE needs no initial conditions on pressure. Furthermore, the components $\hat{f}_x^{+}$ and $\hat{f}_y^{+}$ of $\boldsymbol{\xi}$ coincide with the components $\hat{u}_x^{+}$ and $\hat{v}_y^{+}$ of $\boldsymbol{z}$ in the interior of the domain, but not on the cylinder surface. The computational vector $\boldsymbol{\xi}$, in fact, includes the effects of the boundary conditions on Γ_c and therefore does not vanish there. These characteristics are trivial consequences of the structure of the matrix $\boldsymbol{B}$.

5. Base flow characteristics and code validation

The numerical procedure described in the previous section was used to evaluate the steady flow and to carry out the stability analysis. Calculations were performed on grids of different sizes. The largest domain considered was a $[-25 : 140] \times [-20 : 20]$ rectangle with 900×420 grid points which was particularly valuable for studying the asymptotic structure of the direct eigenfunctions and locating their maxima. However, in order to reduce the computational time and increase the resolution in the near wake, most of the results were obtained on the smaller domain $[-25 : 50] \times [-20 : 20]$ with 600×350 grid points. In all cases, the nodes were smoothly clustered around the cylinder centre according to the transformations (4.1). Refinement tests were

	$Re = 20$		$Re = 40$	
	C_D	L_w	C_D	L_w
Dennis & Chang (1970)	2.05	0.94	1.52	2.35
Coutanceau & Bouard (1977)	...	0.73	...	1.89
Fornberg (1980)	2.00	0.91	1.50	2.24
Ye *et al* (1999)	2.03	0.92	1.52	2.27
Kim *et al.* (2001)	...	...	1.51	...
Current $[-25:50] \times [-20:20]$	2.05	0.92	1.54	2.24

TABLE 1. Drag coefficient C_D and length of the wake bubble L_w (measured from the rear stagnation point).

performed to verify the second-order accuracy of the finite-difference scheme, while the influence of the external boundary conditions on the base flow properties was checked by varying the size of the computational domain. The main characteristics of the steady flow were validated with data available in the literature. As an example, table 1 compares the predicted drag coefficient C_D and the length of the recirculating bubble L_w (measured from the rear stagnation point) obtained from computations at $Re = 20$ and $Re = 40$ with the corresponding values reported by other authors. In order to avoid complications related to the presence of the immersed boundary, C_D was computed from the momentum flux across a rectangle surrounding the cylinder. Results show a reasonable agreement with the most recent numerical computations. The small differences among the values of the drag coefficient are mainly due to the numerical boundary conditions used to solve the nonlinear governing equations. For example, at the inlet, top and bottom boundaries Ye *et al.* (1999) specified the velocity corresponding to the potential flow past a cylinder, whereas here the simpler conditions (4.3*a*) and (4.4*a*) were used. Note that imposing symmetry boundary conditions conceptually corresponds to studying the flow past an infinite array of cylinders. The computed value of C_D, therefore, slowly tends to the real drag coefficient as the width L_y of the computational domain is increased. In any case, the maximum streamwise extent of the separation bubble is predicted well by our technique; as can be seen in figure 6, the size of the recirculating region increases almost linearly with Re, a phenomenon already reported and measured by Zielinska *et al.* (1997). Bearing in mind that the main issue of the paper is the understanding of the global mode structure and not the prediction of the drag coefficient, these results are deemed sufficient validation of the code for the present purposes. As an example of unstable steady flow, figure 5 shows the streamline pattern around the cylinder at $Re = 50$.

6. Stability and receptivity results

The stability characteristics of the base flow are assessed by monitoring the behaviour of the most unstable mode of the linearized equations of motion: to this end it is useful here to remember that the modes of this problem occur in complex conjugate pairs. The critical Reynolds number Re_c at which the steady base flow first becomes unstable was determined by performing a parametric study of the eigenvalue problem (4.9). Figure 7 shows the amplification rate $\mathrm{Re}(\sigma_1)$ and the Strouhal number $St = \mathrm{Im}(\sigma_1)/2\pi$ for the first mode. According to our calculations, the onset of the instability occurs at $Re_c \approx 46.7$, a value which is in good agreement with the numerical results of Jackson (1987), Dušek, Le Gal & Fraunié (1994) and Sheard,

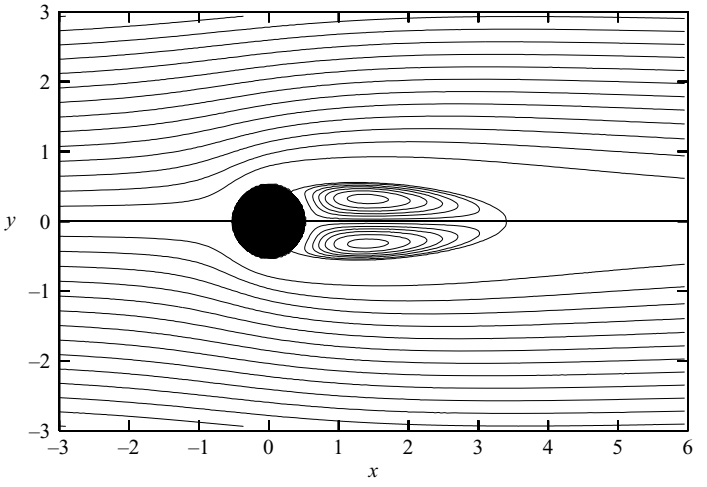

FIGURE 5. Streamlines at $Re = 50$. The isolines outside the separation bubble were produced using a constant contour-level spacing of 0.2, while a spacing of 0.005 was necessary to visualize the slow motion occurring in the recirculating region.

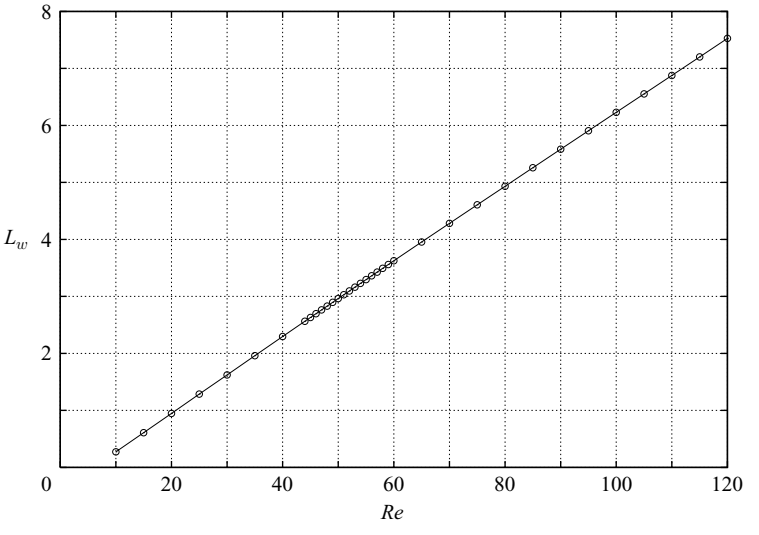

FIGURE 6. Length of the wake bubble (measured from the rear stagnation point) for different Reynolds number.

Thompson & Hourigan (2001) and with the threshold of 47 observed in experiments (Mathis, Provansal & Boyer 1984; Provansal *et al.* 1987; Williamson 1996). The Strouhal number curve has a maximum around $Re \approx 62$, in qualitative agreement with the trend reported by Pier (2002, figure 6, filled circle curve) and obtained through an approximate locally plane-wave analysis (see also figure 16 for a comparison). Note, however, that only in the neighbourhood of the critical point is the predicted Strouhal number in good agreement with the experimental data of Williamson (1996). Linear theory, in fact, is unable to predict the real vortex-shedding frequency in the unstable regime far from the critical point; in these conditions nonlinear effects

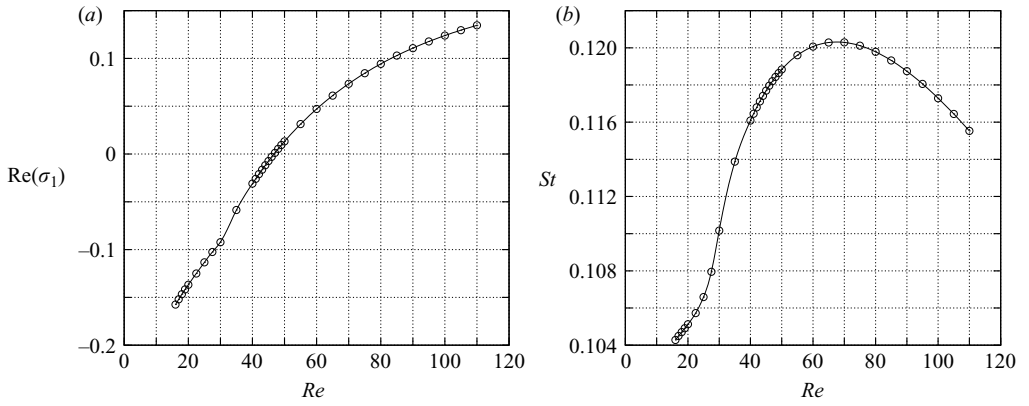

FIGURE 7. (*a*) Amplification-rate and (*b*) Strouhal-number dependence on *Re*.

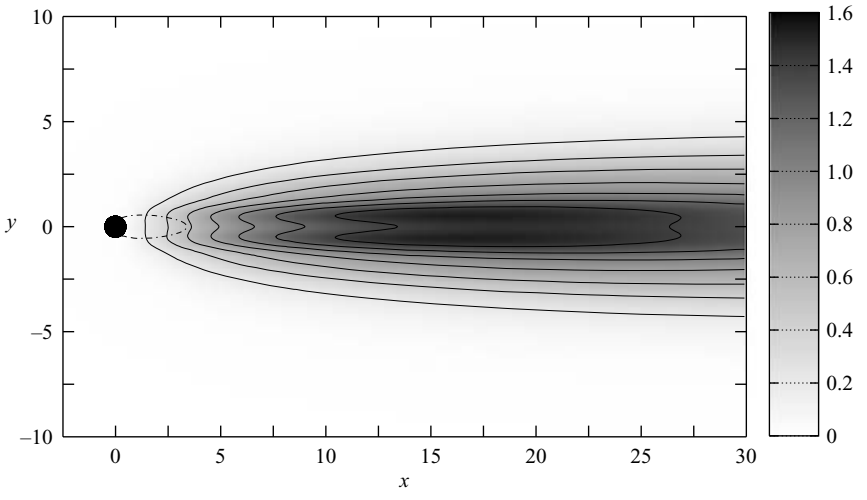

FIGURE 8. Spatial distribution of the velocity field modulus $\|\hat{\boldsymbol{u}}(x, y)\|$ at $Re = 50$.

become important and substantially modify the $St - Re$ relationship away from the linear result of figure 7.

6.1. *Direct and adjoint mode characteristics*

Figures 8 and 9 show the modulus of the velocity $\|\hat{\boldsymbol{u}}(x, y)\|$ and pressure $|\hat{p}(x, y)|$ of the perturbation at $Re = 50$, a value corresponding to a weakly unstable configuration. The dashed line in the pictures indicates the boundary of the separation bubble, while the solid lines are the isolines corresponding to the tick values in the grey-level scale. In the neighbourhood of the critical point, the maxima of $\hat{\boldsymbol{q}}$ are located far downstream of the recirculating region. A surprising fact, in the light of this result, is that both Zebib (1987) and Hill (1992) obtained converged results with a computational domain too short to capture the maxima of the direct eigenfunctions. In their case, the choice of a small domain was mainly dictated by the use of cylindrical coordinates with the ensuing degradation of the spatial resolution with radial distance. The numerical approach used here, on the other hand, allowed us to perform the calculations on a much larger domain: in this way we were able to resolve the details of

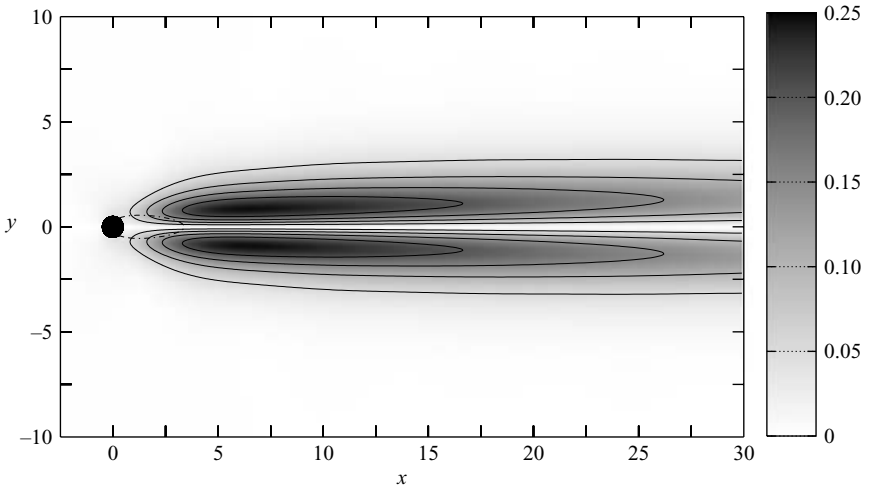

FIGURE 9. Spatial distribution of the pressure modulus $|\hat{p}(x, y)|$ at $Re = 50$.

the far wake and determine the locations of the eigenfunction maxima. In the case of $Re = 50$, the modulus of the velocity reaches its maximum at $x \approx 17$, while the pressure perturbation peaks at $x \approx 6.5$. Beyond these locations, the mode components slowly decay in the streamwise direction. At the outflow boundary, small-amplitude reflected waves are produced by the numerical boundary conditions (4.5*b*). Such waves decay fast in the upstream direction and consequently their influence is limited to a small region located far from the separation bubble. In an attempt to reduce such oscillations, the calculations were repeated implementing the outflow boundary conditions (4.6*b*). Although the computed fields were smoother, the results confirmed that the oscillations have a negligible effect on the global mode structure, as evident from the repeatability of the obtained eigenvalues. An explanation of this unexpected robustness of the eigenvalue computation can be found in the analysis in § 8.

The spatial structure of the global mode changes considerably in the range of Reynolds numbers investigated. The maxima of $\hat{u}$, $\hat{v}$ and $\hat{p}$, in fact, move gradually upstream when Re becomes larger, while the size of the separation bubble tends to increase linearly with it. Goujon-Durand, Jenffer & Wesfreid (1994) and Zielinska & Wesfreid (1995) determined the peak to peak amplitude of the vertical velocity component of the perturbation for the fully nonlinear global mode, obtaining for the position x_{max} of the maximum amplitude of the vortex-shedding envelope the power law $x_{max} \sim (Re - Re_c)^{-1/2}$. This model predicts that the maximum moves farther and farther away from the cylinder as the critical Reynolds number Re_c is approached from above. In the present study, this behaviour is not observed. At $Re = Re_c$, the maximum amplitude of the velocity perturbation is reached approximatively 23 diameters behind the bluff body. The location of the maximum continuously shifts downstream as the Reynolds number is decreased, even for $Re < Re_c$. For $Re \lesssim 43$, we were not able to determine the value of x_{max}; under this threshold, in fact, the maxima lie out of the larger computational domain used to carry out the stability analysis. The disagreement between the behaviour predicted by the power law proposed by Goujon-Durand *et al.* (1994) and the data obtained from our stability analysis is not surprising; the power-law model, in fact, is based on the nonlinear dynamics of the perturbation, whereas the present investigation relies only on a linear approach.

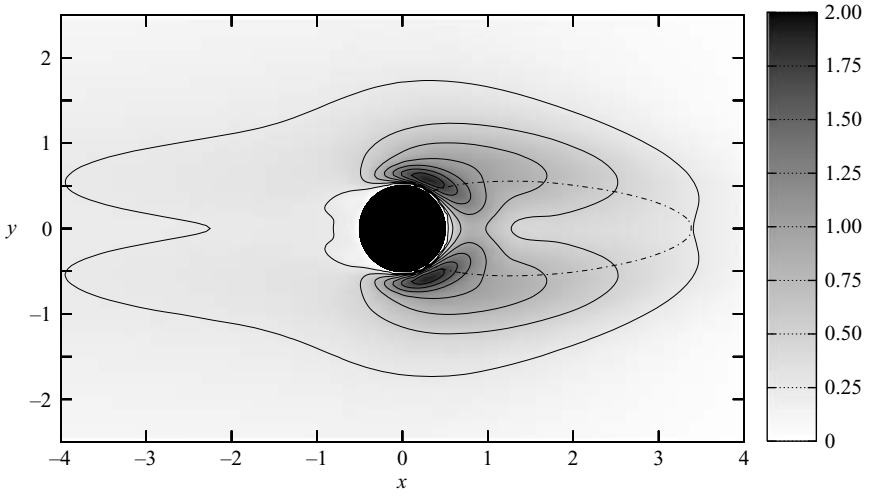

FIGURE 10. Receptivity to momentum forcing and initial conditions ($\|\hat{\boldsymbol{f}}^{+}(x, y)\|$) at $Re = 50$.

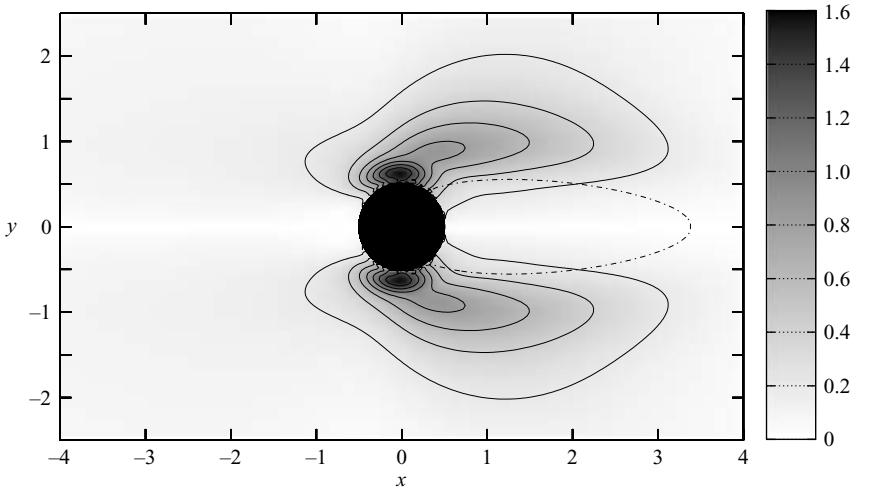

FIGURE 11. Receptivity to mass injection ($|\hat{p}^{+}(x, y)|$) at $Re = 50$.

Both studies, however, predict a shift of x_{max} towards the bluff body as the Reynolds number is increased.

The adjoint mode, on the other hand, shows that the regions of maximum receptivity to momentum forcing and mass injection are localized in the near wake of the cylinder, close to the upper and lower sides of the body surface. This can be seen in figures 10 and 11, which display the spatial distribution of the functions $\|\hat{\boldsymbol{f}}^{+}(x, y)\|$ and $|m^{+}(x, y)|$ at $Re = 50$: darker regions are where the forcing terms $\hat{\boldsymbol{f}}$ and $\hat{m}$ in (3.2) are most effective, i.e. give rise to a mode with the largest amplitude. In striking contrast with the results for the direct mode, the receptivity decays rapidly both upstream and downstream of the cylinder. As discussed in § 3 (and clearly shown in (3.10)), the adjoint field $\hat{\boldsymbol{f}}^{+}(x, y)$ also represents the sensitivity of the mode to the initial conditions used to solve the corresponding temporal stability problem. In particular, modes with large amplitude are produced when the initial conditions

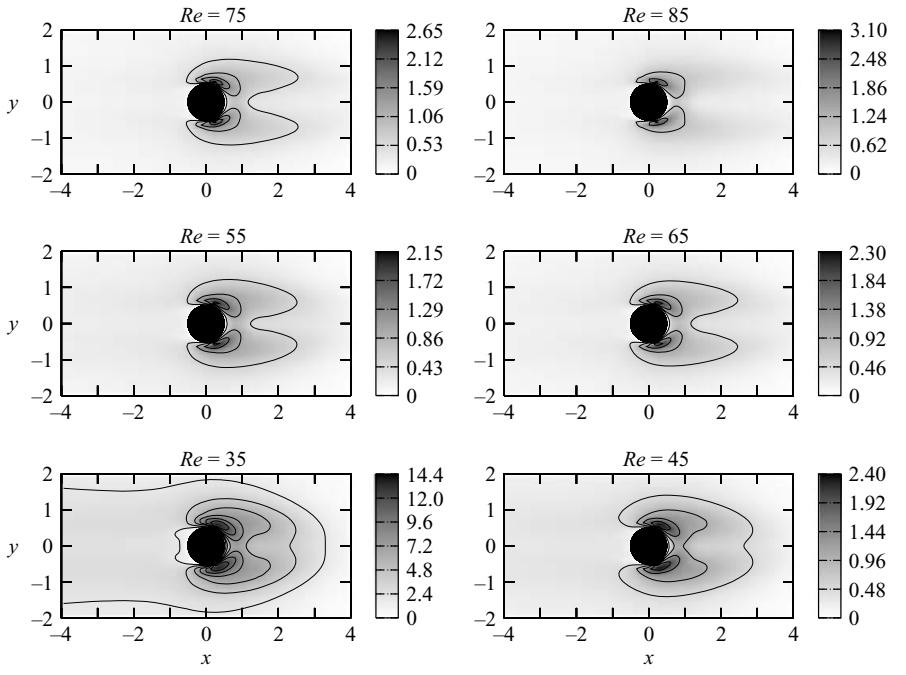

FIGURE 12. Receptivity to momentum forcing and to initial conditions for different Reynolds numbers.

$\boldsymbol{u}_{in}(x, y)$ used to march equations (2.6) are large in correspondence of the darker regions in figure 10. The adjoint fields preserve their spatial characteristics over the range of Reynolds numbers investigated in this paper. This is clearly shown in figure 12, where the receptivity to momentum forcing and to initial conditions is displayed for different Reynolds numbers. A similar behaviour is also found for the receptivity to mass injection.

The large spatial separation of the direct and adjoint field is a consequence of the non-normality of the linearized Navier–Stokes equations which may produce an extreme sensitivity to forcing (Trefethen *et al.* 1993; Schmid & Henningson 2001): for this reason it is important to locate the regions of the flow field which are most receptive to different kinds of forcing mechanisms. The results of this section show that the linearized Navier–Stokes operator for the flow around a cylinder is only moderately non-normal: the values of the components of the adjoint eigenfunction, in fact, are always rather small. A detailed review on the global mode dynamics and non-normality is given by Chomaz (2005).

7. Locally plane-wave analysis

The characteristics of the direct and adjoint modes discussed in the previous section show that the conditions of the flow in the region close to the cylinder wall may have important effects on the temporal evolution of the whole field. Locating the zones where the maximum receptivity is attained it is, however, not sufficient to analyse the process which gives rise to the von Kármán street. The vortex shedding behind bluff bodies, in fact, is generated by a self-exciting mechanism which requires a different approach to be fully understood. In the context of slowly evolving media, for example,

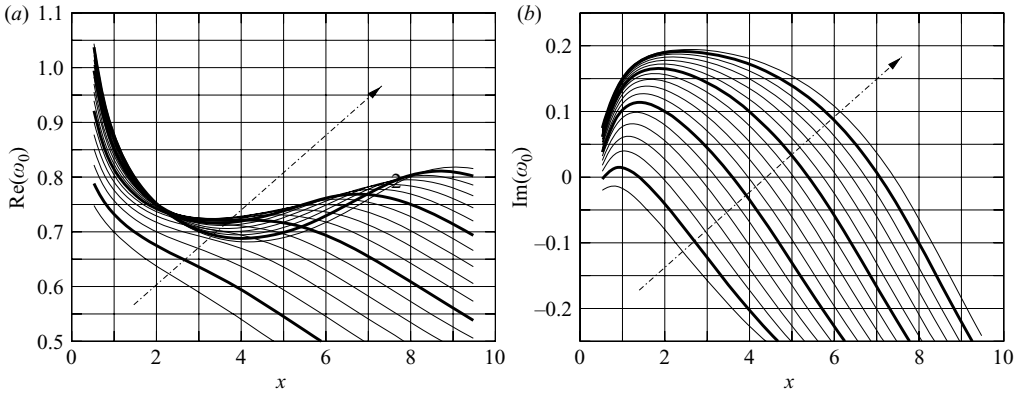

FIGURE 13. (*a*) The real and (*b*) the imaginary part of the absolute frequency ω_0 at different streamwise positions. The Reynolds number corresponding to each curve increases in the direction of the arrow according to the sequence $Re = 20, 25, 30, 35, 40, 45, 50, 55, 60, 65, 70, 75, 80, 85, 90, 95, 100, 105$. (Thick curves pertain to $Re = 25, 50, 75, 100$). The present results are in good agreement with the curves reported in figure 2 of Pier (2002).

the asymptotic theory developed by Chomaz *et al.* (1991), Monkewitz *et al.* (1993) and Le Dizs *et al.* (1996) explains the occurrence of an unstable global mode in terms of the local properties of the flow; relying on the concept of absolute instability, the theory identifies a precise location in the complex x-plane which acts as a wavemaker for the entire field. Although the flow in the cylinder wake is highly non-parallel, Pier (2002) used the asymptotic approach to study the linear and nonlinear dynamics of the instability performing a local analysis, he determined the limits of the absolutely unstable region and determined the position of the 'wavemaker'. In this section, we repeat part of his analysis to evaluate the critical Reynolds number and to locate the position of the complex saddle point. Owing to the high non-parallelism of the base flow it is impossible here to introduce a small inhomogeneity parameter and perform a rigorous analysis based on the separation of the fast scale x, characterizing the instability waves, and the slow scale X over which the base flow experiences an $O(1)$ variation. For this reason, following Pier (2002), we ignore that the present flow is highly non-parallel in the near-wake region and derive the local characteristics at a given streamwise station by freezing the x-coordinate and determining the stability of the parallel shear flow with velocity profile $U_0(y) = U_b(x, y)$. We therefore look for travelling-wave solutions of the form $\boldsymbol{q}(x, y, t) = \hat{\boldsymbol{q}}_l(y)\exp(\mathrm{i}\omega t - \mathrm{i}kx)$, where ω is the frequency and k is the streamwise wavenumber of the disturbance. These waves are governed by the Orr–Sommerfeld equation (Drazin & Reid 1981) which yields the local linear dispersion relation $\omega = \Omega^l(k, x)$ between the complex frequency ω and the complex wavenumber k at the streamwise station x under consideration. The resulting linear eigenvalue problems in the cross-stream coordinate are solved with the inverse iteration algorithm introduced for the two-dimensional stability analysis. The complex absolute frequency $\omega_0(x)$ is found by applying the zero group velocity condition

$$\omega_0(x) = \Omega(k_0, x) \quad \text{with} \quad \left(\frac{\partial \Omega}{\partial k}\right)_{k=k_0} = 0 \tag{7.1}$$

on the local linear dispersion relation (Briggs 1964; Bers 1975). Figure 13 shows the streamwise evolution of the absolute growth rate $\mathrm{Im}(\omega_0)$ and the real absolute frequency $\mathrm{Re}(\omega_0)$ for different values of the Reynolds number. Asymptotic theory

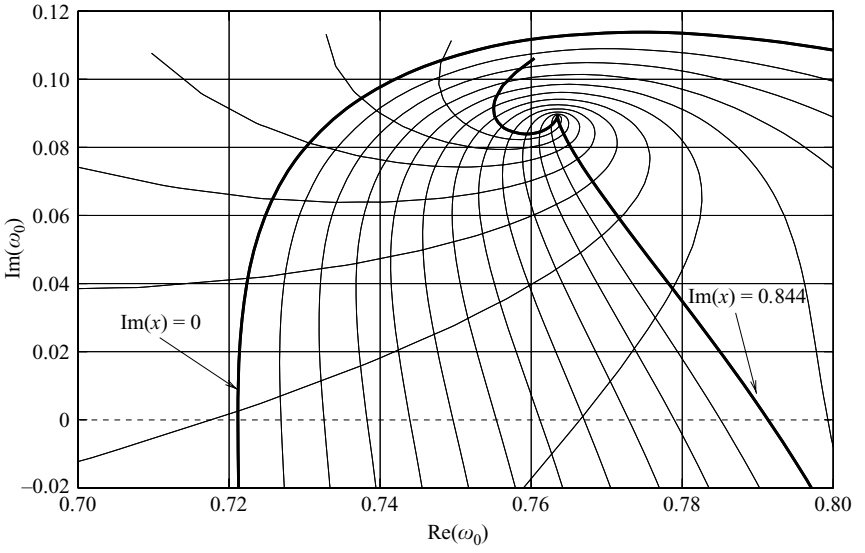

FIGURE 14. Localization of the saddle point of the dispersion relation in the complex x-plane at $Re = 50$. Different curves correspond to different value of $\mathrm{Im}(x)$. Thick curves pertain to $\mathrm{Im}(x) = 0$ and $\mathrm{Im}(x) = 0.844$.

predicts that a global mode can occur only if a sufficiently large region of absolute instability exists. Results reveal that local absolute instability ($\mathrm{Im}(\omega_0) > 0$) prevails downstream of the obstacle when $Re > 25$, in agreement with the numerical computations of Yang & Zebib (1988). The complex global frequency ω_g is evaluated by imposing the saddle-point condition

$$\omega_g = \omega_0(x_s) \quad \text{with} \quad \frac{\partial \omega_0}{\partial x}(x_s) = 0 \tag{7.2}$$

on the analytic continuation of the local absolute frequency curve $\omega_0(x)$ in the complex x-plane. Following Cooper & Crighton (2000), the computed absolute frequency data are interpolated by a rational function $P^n(x)/Q^n(x)$, where $P^n(x)$ and $Q^n(x)$ are polynomials whose degree is at most n. The saddle point is then found by using a Newton iteration. Calculations repeated for values of n ranging from 6 to 30 show a substantial independence of x_s from the order of the polynomials. To verify the results, the singularity is also detected graphically by plotting the absolute frequency curves for different values of the imaginary part x_i of the streamwise coordinate and determining the value for which a cusp formation, corresponding to the point where $(\partial\omega_0/\partial x)(x_s) = 0$, is visible in the complex ω-plane (see figure 14 for an example at $Re = 50$). Finally, the global frequency ω_g is calculated by (7.2) for different Reynolds numbers. Figure 15 displays the variation of the real and imaginary part of x_s with Re; for the configuration studied, the complex saddle point is always located quite far from the real axis. Figure 16 displays the growth rate and the Strouhal number predicted by the asymptotic theory for the cylinder wake at different Reynolds numbers. In order to ease the comparison, data obtained in previous numerical and experimental investigations are also reported in the same graphs. The results for the frequency compare well with those obtained by Pier (2002) through a local analysis. The curves for both the frequency and the Strouhal number show trends qualitatively similar to those derived through the two-dimensional global analysis. However, a more detailed

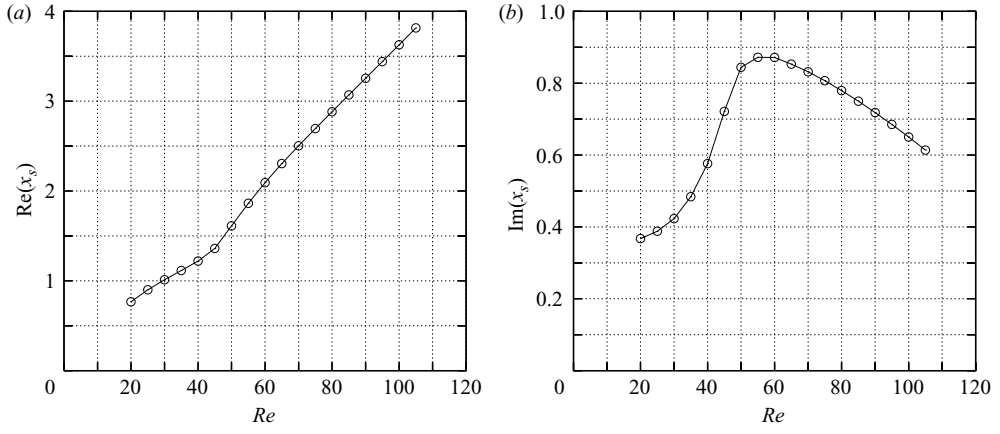

FIGURE 15. Variation of the saddle-point location x_s in the complex x-plane with the Reynolds number.

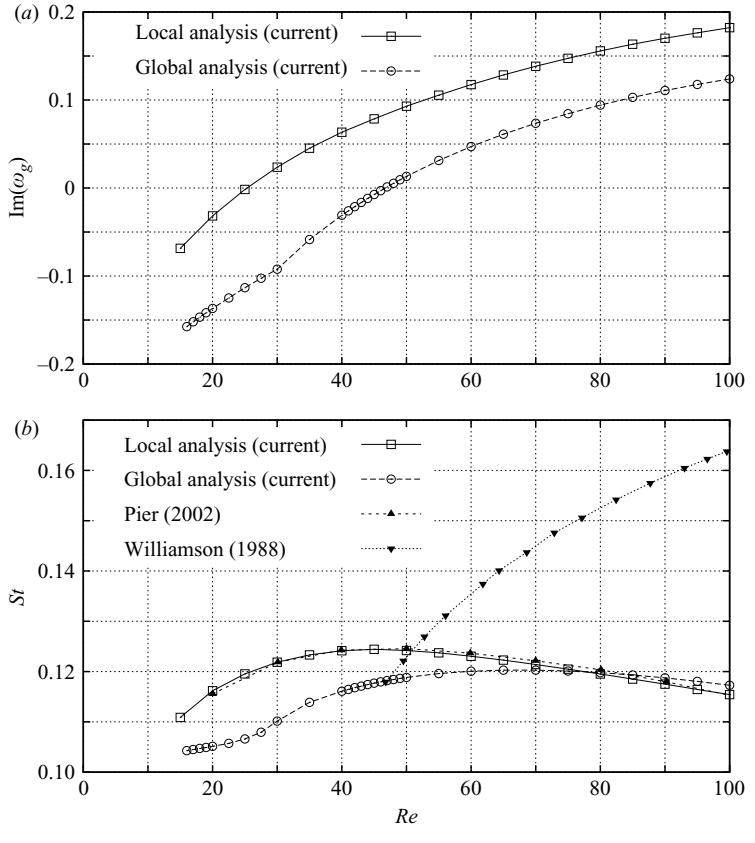

FIGURE 16. (*a*) Growth rate and (*b*) Strouhal number predicted by local theory for the cylinder wake at different Reynolds numbers. Results obtained by a global bidimensional analysis, the vortex-shedding frequencies determined by Pier (2002) through local theory and the experimental Strouhal curve from Williamson (1988) are also shown in the graphs for comparison.

inspection reveals that the quantitative agreement between the two sets of data is poor. Local analysis, for example, predicts the occurrence of an unstable global mode at $Re \approx 26$, underestimating considerably the value of the critical Reynolds number. Moreover the Strouhal number curve peaks at Reynolds number $Re \approx 45$, whereas the maximum for the data derived through the bidimensional stability analysis is reached at about $Re = 62$. These results confirm that a locally plane-wave analysis is not suited to performing a precise quantitative study of the instability in the wake of the cylinder, where non-parallel effects are $O(1)$. Nevertheless, the asymptotic approach can be useful for obtaining a qualitative picture of the self-exciting process generating the vortex street and for approximately locating the regions in the real (x, y)-plane where the instability mechanism acts. From a qualitative point of view, considering only the real part of x_s and observing where the absolute growth rate curve $\omega_0(x)$ reaches its maximum value, it is reasonable to suppose that the core of the instability is placed in the middle of the separation bubble, at an intermediate distance between the wall of the cylinder and the re-attachment point. In the next section, using a novel technique based on a structural stability analysis of the LNSE, we will determine precisely the instability core and we will verify the qualitative predictions based on the asymptotic approach.

8. Determination of the instability core: receptivity to spatially localized feedbacks

The large difference betweens the spatial structure of the two-dimensional direct and adjoint modes described in § 6.1 suggests that the instability mechanism cannot be identified from the study of either eigenfunctions separately. The asymptotic theory developed by Chomaz *et al.* (1991), Monkewitz *et al.* (1993) and Le Dizès *et al.* (1996) in the context of slowly evolving quasi-parallel flows, endows the region around the saddle point with the fundamental role of 'wavemaker' in the excitation of the global mode. In the context of a two-dimensional modal analysis, a concept similar to that of 'wavemaker' can be introduced by investigating where in space a modification in the structure of the problem is able to produce the greatest drift of the eigenvalue. This being the case, in fact, it would be justified to claim that the structural perturbation has hit the 'core' of the instability mechanism. This point can be explained better in the context of a finite dimensional system. Let us consider a generalized eigenvalue problem of the form

$$[\boldsymbol{A} + \sigma_1 \boldsymbol{B}] \cdot \boldsymbol{w} = \boldsymbol{0}, \tag{8.1}$$

and introduce a small perturbation $\delta \boldsymbol{A}$ of the operator $\boldsymbol{A}$. The eigenvalue drift $\delta\sigma_1$, due to the structural perturbation $\delta \boldsymbol{A}$, is readily obtained by performing the differential

$$\delta\{[\boldsymbol{A} + \sigma_1 \boldsymbol{B}] \cdot \boldsymbol{w}\} = [\delta \boldsymbol{A} + \delta\sigma_1 \boldsymbol{B}] \cdot \boldsymbol{w} + [\boldsymbol{A} + \sigma_1 \boldsymbol{B}] \cdot \delta \boldsymbol{w} \tag{8.2}$$

and dot multiplying the result with the adjoint eigenvector $\boldsymbol{\xi}$. In this way, recalling that $\boldsymbol{\xi} \cdot (\boldsymbol{A} + \sigma_1 \boldsymbol{B}) = \boldsymbol{0}$, we easily obtain the simple relation

$$\delta\sigma_1 = -\frac{\boldsymbol{\xi} \cdot \delta \boldsymbol{A} \cdot \boldsymbol{w}}{\boldsymbol{\xi} \cdot \boldsymbol{B} \cdot \boldsymbol{w}}. \tag{8.3}$$

Note that the sensitivity of the eigenvalue (and in general of the entire spectrum) depends on the level of non-normality of the linear operator $\boldsymbol{A}$ (see Chomaz 2005 for a detailed discussion). In cases in which the perturbation operator $\delta \boldsymbol{A}$ has only one non-vanishing element, say for example the element $\delta a_{m,n}$, (8.3) can be further

simplified to give

$$\delta\sigma_1 = -\frac{\sum_{i,j} \xi_i \delta a_{i,j} w_j}{\boldsymbol{\xi}\cdot\boldsymbol{B}\cdot\boldsymbol{w}} = -\frac{\xi_m w_n}{\boldsymbol{\xi}\cdot\boldsymbol{B}\cdot\boldsymbol{w}}\delta a_{m,n} = \frac{\partial\sigma_1}{\partial a_{m,n}}\delta a_{m,n}. \tag{8.4}$$

This expression shows that the product between the components of the direct and adjoint eigenfunctions is the Green's function for the eigenvalue perturbation induced by an infinitesimal disturbance $\delta a_{m,n}$ of the operator $\boldsymbol{A}$. In our case the operators $\boldsymbol{A}$ and $\boldsymbol{B}$ are the matrices derived from the discretization of the stability problem (2.10), while the vectors $\boldsymbol{w}$ and $\boldsymbol{\xi}$ are, respectively, approximations of the direct and adjoint modes. When the perturbations are localized in space, then only a few elements of $\delta\boldsymbol{A}$ are different from zero. An expression similar to (8.4) can also be derived for the differential problem (2.10). Consider, in fact, the perturbed eigenvalue problem satisfying equations

$$\sigma_1'\hat{\boldsymbol{u}}' + \boldsymbol{L}\{\boldsymbol{U}_b, Re\}\hat{\boldsymbol{u}}' + \nabla\hat{p}' = \delta\boldsymbol{H}(\hat{\boldsymbol{u}}', \hat{p}'), \tag{8.5a}$$

$$\nabla\cdot\hat{\boldsymbol{u}}' = \delta R(\hat{\boldsymbol{u}}', \hat{p}'), \tag{8.5b}$$

along with homogeneous boundary conditions. Here $\delta\boldsymbol{H}$ and $\delta\boldsymbol{R}$ denote two linear differential operators expressing the structural perturbation of the original differential problem, while primes indicate quantities satisfying the perturbed equations. The eigenvalue drift $\delta\sigma_1$ and the eigenfunction perturbation $\delta\hat{\boldsymbol{q}} \equiv \{\delta\hat{\boldsymbol{u}}, \delta\hat{p}\}$ can be related using a simple expansion in terms of the solution of the unperturbed problem. Assuming $\hat{\boldsymbol{u}}' = \hat{\boldsymbol{u}} + \delta\hat{\boldsymbol{u}}$, $\hat{p}' = \hat{p} + \delta\hat{p}'$ and $\sigma_1' = \sigma_1 + \delta\sigma_1$, inserting into (8.5) and neglecting quadratic terms, we easily obtain

$$\sigma_1\ \delta\hat{\boldsymbol{u}} + \boldsymbol{L}\{\boldsymbol{U}_b, Re\}\delta\hat{\boldsymbol{u}} + \nabla\delta\hat{p} = -\delta\sigma_1\hat{\boldsymbol{u}} + \delta\boldsymbol{H}(\hat{\boldsymbol{u}}, \hat{p}), \tag{8.6a}$$

$$\nabla\cdot\boldsymbol{\delta}\hat{u} = \delta R(\boldsymbol{u}, p). \tag{8.6b}$$

Applying the Lagrange identity to the perturbation field $\delta\boldsymbol{q}(x, y) = \delta\hat{\boldsymbol{q}}(x, y)\exp(\sigma_1 t)$ and to the adjoint mode $\boldsymbol{g}^+(x, y) = \hat{\boldsymbol{g}}^+(x, y)\exp(-\sigma_1 t)$ corresponding to the eigenvalue σ_1, integrating over the domain $\mathscr{D}$, using (8.6) and taking into account the boundary conditions, we arrive at:

$$\delta\sigma_1 = \frac{\int_D \hat{\boldsymbol{f}}_1^+\cdot\delta\boldsymbol{H}(\hat{\boldsymbol{u}}_1, \hat{p}_1) + \hat{m}^+\delta R(\hat{\boldsymbol{u}}_1, \hat{p}_1)\,\mathrm{d}S}{\int_{\mathscr{D}} \hat{\boldsymbol{f}}_1^+\cdot\hat{\boldsymbol{u}}_1\,\mathrm{d}S}, \tag{8.7}$$

relating the eigenvalue drift to the perturbation operators and the adjoint field. This approach is used here to investigate the structural stability of the flow around a circular cylinder. Equation (8.7) is valid for a generic structural perturbation: the associated shift in the eigenvalue can be calculated once the operators $\delta\boldsymbol{H}$ and δR are specified. As for the finite-dimensional problem, (8.7) can be further simplified if we consider structural perturbations localized in space. These may arise for several different reasons, including changes in the base flow, in the body geometry or even in the numerical boundary conditions imposed to solve the stability problem. As an example, we consider here the effects induced by the existence of a spatially localized feedback. More precisely, we investigate the sensitivity of the eigenvalue $\delta\sigma_1$ with respect to a generic force–velocity coupling. Such a feedback could be in theory produced by introducing in the flow field a small device which exerts on the fluid a force whose direction and strength depend on the local value of the velocity

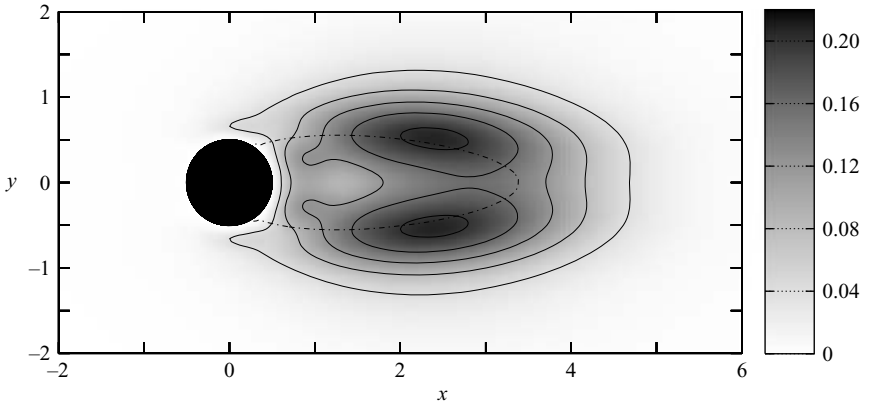

FIGURE 17. Receptivity to spatially localized feedbacks at $Re = 50$.

perturbation. In a sense, a similar mechanism can be considered as the 'wavemaker' of the asymptotic theory. In a linear theory approach, the feedback process can be mathematically described through a relation of the form

$$\boldsymbol{f} = \boldsymbol{C}(x, y) \cdot \boldsymbol{u} \tag{8.8}$$

where $\boldsymbol{C}$ is the 2×2 matrix of the coupling coefficients, while $\boldsymbol{u}$ and $\boldsymbol{f}$ are the velocity and the force fields in (2.6). Generally, the coupling coefficients in the matrix are functions of the coordinates (x, y). However, if the feedback is localized in space, we can simplify the model by assuming

$$\boldsymbol{C}(x, y) = \delta(x - x_0, y - y_0)\boldsymbol{C}_0, \tag{8.9}$$

where $\boldsymbol{C}_0$ is here a constant coefficient matrix, (x_0, y_0) indicates the position where the feedback acts and $\delta(x - x_0, y - y_0)$ denotes the Kronecker delta function. A bound for the eigenvalue drift due to the localized feedback mechanism can be derived by considering the Laplace transform of (8.8) and taking $\delta \boldsymbol{H}(\hat{\boldsymbol{u}}, \hat{p}) = \boldsymbol{C}(x, y) \cdot \hat{\boldsymbol{u}}$ and $\delta R(\hat{\boldsymbol{u}}, \hat{p}) = 0$ in (8.7). In this way, using (8.9), we obtain

$$|\delta\sigma_1| = \frac{\left| \displaystyle\int_D \hat{\boldsymbol{f}}^+ \cdot \boldsymbol{C}(x, y) \cdot \hat{\boldsymbol{u}} \, \mathrm{d}S \right|}{\left| \displaystyle\int_{\mathscr{D}} \hat{\boldsymbol{f}}^+ \cdot \hat{\boldsymbol{u}} \, \mathrm{d}S \right|} \leqslant \|\boldsymbol{C}_0\| \lambda(x_0, y_0) \tag{8.10}$$

where we have defined the function $\lambda(x, y)$ as

$$\lambda(x, y) = \left| \frac{\|\hat{\boldsymbol{f}}^+(x, y)\| \|\hat{\boldsymbol{u}}(x, y)\|}{\displaystyle\int_{\mathscr{D}} \hat{\boldsymbol{f}}^+ \cdot \hat{\boldsymbol{u}} \, \mathrm{d}S} \right|. \tag{8.11}$$

Equation (8.10) shows that the product between the direct and adjoint fields gives the maximum possible coupling among the velocity components. The function $\lambda(x, y)$ can therefore be used to determine the locations where the feedback is stronger, identifying in this way the regions where the instability mechanism acts. Figure 17 shows that large values of $\lambda(x, y)$ are attained in two lobes located symmetrically across the separation bubble. Note that both close to the cylinder and far from it, the product of the adjoint and direct modes is small, showing that these areas of the flow are not really important for the instability dynamics.

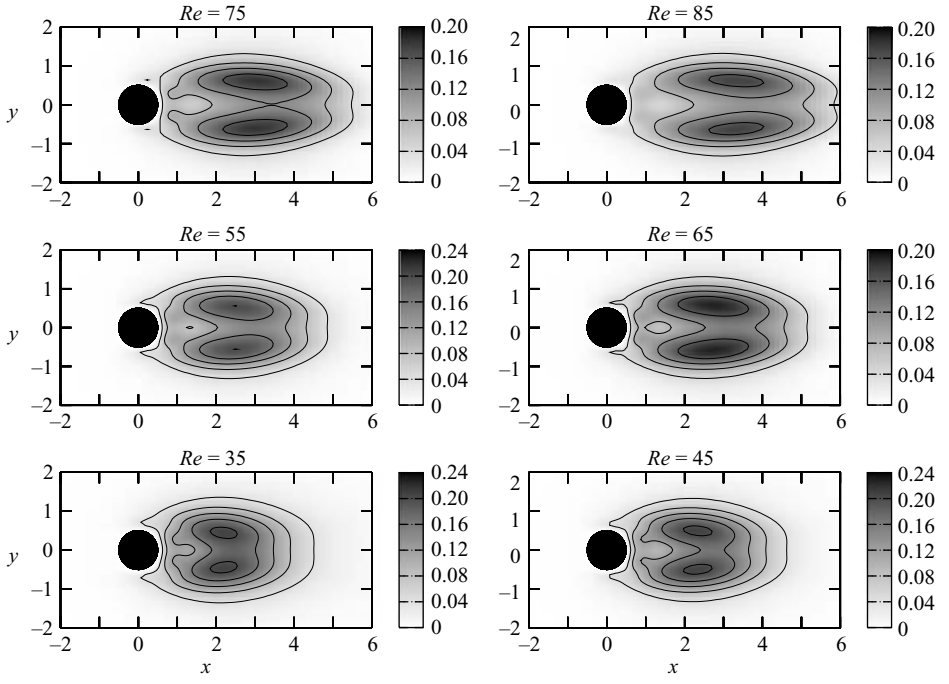

FIGURE 18. Contour plot of the function $\lambda(x, y)$ at different Reynolds numbers.

If the Reynolds number is increased, the spatial separation between the maxima of the direct and adjoint modes is reduced, but the main characteristics of $\lambda(x, y)$ remain unaltered. As figure 18 shows, in fact, the maxima of $\lambda(x, y)$ are always located in two symmetric lobes across the separation bubble and slowly move downstream when the value of Re is increased. In the cases considered, however, the maxima lie at a distance from the cylinder wall smaller than the recirculation length L_w (see also figure 6).

8.1. *Sensitivity of the eigenvalue*

The spatial distribution of the product between the direct and adjoint eigenfunctions suggests that the characteristics of the global mode are dictated mainly by the conditions existing in the region where values of $\lambda(x, y)$ substantially different from zero are attained. In order to check this hypothesis, the stability analysis can be repeated on progressively shortened domains in order to verify the influence of the different regions of the flow on the eigenvalue. Note that the problem of determining the sensitivity of σ_1 to the size of the computational domain naturally fits in a structural stability framework; resizing the domain, in fact, is substantially equivalent to changing the boundary conditions of the discretized problem. The numerical results are in good qualitative agreement with the predictions based on the spatial analysis of the product between the direct and adjoint modes and show that the eigenvalue varies significantly only when the boundary conditions are placed in the proximity of the regions in which $\lambda(x, y)$ is significantly different from zero. As an example, table 2 gives the values of σ_1 obtained by performing the stability analysis on several restricted domains. Until the instability core is included inside the computational boundaries, the eigenvalue drift remains relatively small. The spatial structure of the mode is also substantially preserved. This can be seen in figure 19 which compares the

Domain size	Eigenvalue σ_1
$[-25:+50]\times[-20:+20]$	$0.01295+0.75022i$
$[-10:+10]\times[-10:+10]$	$0.01398+0.75152i$
$[-5.0:+10]\times[-5.0:+5.0]$	$0.01507+0.75040i$
$[-4.0:+9.0]\times[-3.0:+3.0]$	$0.02196+0.75318i$
$[-2.5:+8.0]\times[-2.5:+2.5]$	$0.02692+0.76852i$
$[-1.0:+7.0]\times[-2.5:+2.5]$	$0.00208+0.80386i$

TABLE 2. Eigenvalue sensitivity to the size of the computational domain.

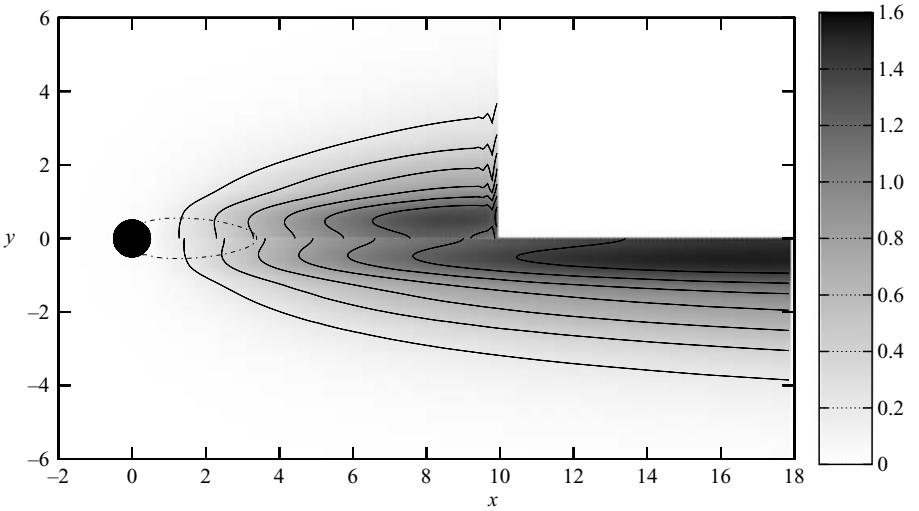

FIGURE 19. Spatial distribution of the velocity modulus at $Re=50$ obtained on a $[-10:10]\times[-10:10]$ computational domain (upper part) and on the larger domain $[-25:50]\times[-20:20]$ (lower part). Figures are symmetric with respect to $y=0$.

modulus of the velocity obtained from a computation on a $[-10:10]\times[-10:10]$ grid with the results obtained on the larger domain $[-25:50]\times[-20:20]$. The wiggles at the outflow boundary are due to reflected waves produced by the outflow numerical boundary conditions. Such waves are confined in a narrow strip and do not modify the main characteristics of the mode. As expected, imposing the inflow conditions near the cylinder surface is less effective than setting the outflow boundary across the separation bubble. Even when the cylinder is excluded from the computational domain, a reasonable value for σ_1 can still be found. A similar behaviour was also noticed by Triantafyllou & Karniadakis (1990) who numerically reproduced a vortex street by using a computational domain restricted to the region downstream of the obstacle. These results confirm the qualitative predictions based on asymptotic theory and show that the core of the instability is located behind the cylinder, almost at the end of the recirculating region. Furthermore, this approach explains why the calculations of Zebib (1987) and Hill (1992) gave the correct results despite the small computational domain used.

8.2. *Comparison with experiments and relevance to vortex shedding control*

In order to validate the results obtained through the structural stability analysis and show the relevance of this new technique to the control problem, we compare

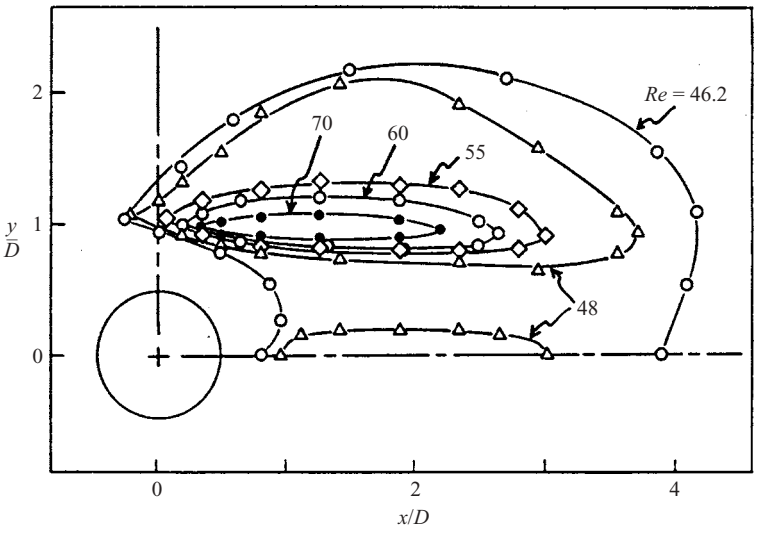

FIGURE 20. Locus in the (x, y)-plane where the placement of the small control cylinder results in a zero growth rate ($\mathrm{Re}(\sigma_1) = 0$) of the temporal mode (from Strykowski & Sreenivasan 1990).

our theoretical predictions with the experimental and numerical data obtained by Strykowski & Sreenivasan (1990). As noticed by Chomaz (2005), in fact, the structural stability prediction agrees qualitatively well with the numerical and experimental data obtained by these authors. In an attempt to control the von Kármán street they placed a second, much smaller, control cylinder in the near wake of the main cylinder and noticed that in choosing a proper placement the vortex shedding was considerably altered and even suppressed altogether over a limited range of Reynolds numbers. Temporal growth rate measurements of the velocity fluctuations revealed that the presence of the smaller cylinder reduces the growth rate of the disturbances leading to vortex shedding and that its suppression, accompanied by the disappearance of sharp spectral peaks, coincides with negative temporal growth rates. Experimental results were substantiated by numerical investigations performed by solving the incompressible Navier–Stokes equations. The results confirmed the existence of two finite spatial domains symmetrically placed about the line $y = 0$ within which the placement of the control cylinder can suppress the vortex street. The shape of these regions depends on the ratio $\kappa = D^*/d^*$ between the diameters of the main and secondary cylinder and shrinks with increasing κ. When the control cylinder was placed anywhere within these regions, the vortex street was suppressed completely. At $Re = 80$, the largest value of the diameter ratio which was capable of vortex suppression was $\kappa = 10$. Experiments conducted in a low-turbulence wind tunnel with blockage ratio $H/D = 60$ (H is here the width of the wind-tunnel test section) showed that for $\kappa = 10$, complete suppression is possible for Reynolds number up to 80. For larger values of Re, the vortex shedding was still visible, but the growth rate of the disturbances was considerably smaller than in the uncontrolled case. Strykowski & Sreenivasan (1990) represented the influence of the control cylinder for different Reynolds numbers by plotting the locus of all points in the (x, y)-plane corresponding to a zero growth rate (figure 20). As the Reynolds number is increased, we reach a value at which the contours shrink to a point. In this case, the position of the control cylinder is critical and suppression at higher Reynolds numbers is impossible.

The results of this experiment can be explained in terms of the structural stability analysis previously set forth. The placement of a small cylinder in the near wake of a bluff body, in fact, results in a reaction force acting on the fluid which modifies the flow field and leads to a shift of the eigenvalue σ_1. Since the control cylinder is small, its presence can be thought of as a localized structural perturbation of the linearized governing equations consisting in a localized feedback from velocity to force. Comparing figures 17 and 20, we notice a striking similarity between the two results. Considering that the secondary cylinder used in the experiment has a small but finite radius, the agreement between the theoretical predictions and the experimental data is qualitatively good. In particular, note how the regions where the placement of the control cylinder produces the maximum effect are well determined by the analysis based on the product between the direct and the adjoint mode. As observed by Strykowski & Sreenivasan (1990), placing the secondary cylinder downstream of these regions is not effective for vortex-shedding suppression, confirming in this way that the core of the instability lies in a region located 3–4 diameters downstream of the main cylinder. This example shows how the technique based on the structural stability analysis of the governing equations can be used to design efficient control strategies for the vortex shedding behind bluff bodies.

9. Summary and conclusions

In this paper, we perform a stability analysis of the flow around a circular cylinder using linear theory. An immersed boundary technique is used to represent the body surface on a Cartesian mesh. The stability properties of the base flow are analysed by solving numerically a two-dimensional generalized eigenvalue problem. The spatial structure of both the direct and adjoint modes is investigated, and the regions of the flow most sensitive to momentum forcing and mass injection are located. The analysis shows that the maximum of the perturbation envelope amplitude is reached far downstream of the separation bubble, whereas the highest receptivity is attained in the near wake of the cylinder, close to the body surface, in agreement with Hill (1992). The large difference between the spatial structure of the two-dimensional direct and adjoint modes, owing to the non-normality of the linearized Navier–Stokes operator, suggests that the instability mechanism cannot be identified from the study of either eigenfunctions separately. A structural stability analysis is therefore performed in order to understand better the mechanism which is at the base of the self-sustained mode. In particular, the core of the instability is identified by inspecting the spatial structure of the product between the direct and adjoint eigenfunctions. This quantity takes into account the 'feedback' which is at the origin of the self-excited oscillation and is therefore useful to locate the region of the flow which acts as a 'wavemaker'. We found that the maximum possible coupling among the velocity components is obtained approximately at the end of the separation bubble, in two regions located symmetrically across the line of symmetry of the base flow. Our results confirm the qualitative predictions of the asymptotic theory, in spite of its application being justified in principle only in media with slowly evolving properties. The technique introduced here, on the other hand, accounts for strong non-parallel effects and can therefore be used to investigate the nature of complex flow configurations and to locate the regions where the instability mechanism acts. The theoretical predictions based on the structural stability analysis compare well with the experimental and numerical data of Strykowski & Sreenivasan (1990), showing the relevance of this novel technique to the development of effective control strategies for vortex shedding behind bluff bodies.

A preliminary version of this work as been presented as a poster at the 5th Euromech Fluid Mechanics Conference (EFMC) held in Toulouse, France on 24–28 August 2003.

REFERENCES

Barkley, D. & Henderson, R. 1996 Three-dimensional Floquet stability analysis of the wake of a circular cylinder. *J. Fluid Mech.* **322**, 215–241.

Bender, C. M. & Orszag, S. A. 1978 *Advanced Mathematical Methods for Scientists and Engineers*. McGraw-Hill.

Bers, A. 1975 Linear waves and instabilities. In *Physique des Plasmas* (ed. C. DeWitt & J. Peyraud), pp. 113–215. Gordon & Breach.

Blackburn, H. M. & Henderson, R. D. 1999 A study of two-dimensional flow past an oscillating cylinder. *J. Fluid Mech.* **385**, 255–286.

Briggs, R. 1964 *Electron-Stream Interaction with Plasmas*. MIT Press.

Chomaz, J.-M. 2005 Global instabilities in spatially developing flows: non-normality and nonlinearity. *Annu. Rev. Fluid Mech.* **156**, 209–240.

Chomaz, J.-M., Huerre, P. & Redekopp, L. 1991 A frequency selection criterion in spatially developing flows. *Stud. Appl. Maths* **84**, 119–144.

Cooper, A. J. & Crighton, D. G. 2000 Global modes and superdirective acoustic radiation in low-speed axisymmetrics jets. *Eur. J. Mech.* B/*Fluids* **19**, 559–574.

Coutanceau, M. & Bouard, R. 1977 Experimental determination of the main features of the viscous flow in the wake of a circular cylinder in uniform translation. Part 1. Steady flow. *J. Fluid Mech.* **79**, 231–256.

Dennis, S. R. C. & Chang, G. 1970 Numerical solutions for steady flow past a circular cylinder at Reynolds number up to 100. *J. Fluid Mech.* **42**, 471–489.

Drazin, P. G. & Reid, W. H. 1981 *Hydrodynamic Stability*. Cambridge University Press.

Dušek, J., Le Gal, P. & Fraunié, P. 1994 A numerical and theoretical study of the first Hopf bifurcation in a cylinder wake. *J. Fluid Mech.* **264**, 59–80.

Fadlun, E. A., Verzicco, R., Orlandi, P. & Mohd-Yusof, J. 2000 Combined immersed-boundary finite-difference methods for three-dimensional complex flow simulations. *J. Comput. Phys.* **161**, 35–60.

Fornberg, B. 1980 A numerical study of steady viscous flow past a circular cylinder. *J. Fluid Mech.* **98**, 819–855.

Golub, G. H. & Van Loan, C. 1989 *Matrix Computations*, 2nd edn. Johns Hopkins University Press.

Goujon-Durand, S., Jenffer, P. & Wesfreid, J. E. 1994 Downstream evolution of the Bénard–von Kármán instability. *Phys. Rev. Lett.* **50**, 308–313.

Hill, D. C. 1992 A theoretical approach for analyzing the re-stabilization of wakes. *AIAA Paper* 92-0067.

Hinch, E. J. 1994 *Perturbation Methods*. Cambridge University Press.

Huerre, P. & Monkewitz, P. A. 1985 Absolute and convective instabilities in free shear layers. *J. Fluid Mech.* **159**, 151–168.

Huerre, P. & Monkewitz, P. A. 1990 Local and global instabilities in spatially developing flows. *Annu. Rev. Fluid Mech.* **22**, 473–537.

Ince, E. L. 1926 *Ordinary Differential Equations*. Dover.

Jackson, C. P. 1987 A finite-element study of the onset of vortex shedding in flow past variously shaped bodies. *J. Fluid Mech.* **182**, 23–45.

Karniadakis, G. E. & Triantafyllou, G. S. 1992 Three-dimensional dynamics and transition to turbulence in the wakes of bluff bodies. *J. Fluid Mech.* **238**, 1–30.

Kim, J., Kim, D. & Choi, H. 2001 An immersed-boundary finite-volume method for simulations of flow in complex geometries. *J. Comput. Phys.* **171**, 132–150.

Le Dizès, S., Huerre, P., Chomaz, J.-M. & Monkewitz, P. A. 1996 Linear global modes in spatially developing media. *Phil. Trans. R. Soc. Lond.* **354**, 169–212.

Mathis, C., Provansal, M. & Boyer, L. 1984 Bénard–von Kármán instability: an experimental study near the threshold. *J. Phys. Lett. Paris* **45**, 483–491.

Mittal, R. & Balachandar, S. 1996 Direct numerical simulation of flow past elliptic cylinders. *J. Comput. Phys.* **124**, 351–367.

Mohd-Yusof, J. 1997 Combined immersed-boundary/B-spline methods for simulations of flows in complex geometries. Annu. Res. Briefs. Center for Turbulence Research, NASA Ames and Standford University, p. 317.

Monkewitz, P. A., Huerre, P. & Chomaz, J.-M. 1993 Global linear stability analysis of weakly non-parallel shear flows. *J. Fluid Mech.* **251**, 1–20.

Morse, P. M. & Feshbach, H. 1953 *Methods of Theoretical Physics*. McGraw-Hill.

Noack, B. R. & Eckelmann, H. 1994 A global stability analysis of the steady and periodic cylinder wake. *J. Fluid Mech.* **270**, 297–330.

Pier, B. 2002 On the frequency selection of finite-amplitude vortex shedding in the cylinder wake. *J. Fluid Mech.* **458**, 407–417.

Provansal, M., Mathis, C. & Boyer, L. 1987 Bénard–von Kármán instability: transient and forced regimes. *J. Fluid Mech.* **182**, 1–22.

Schmid, P. J. & Henningson, D. S. 2001 *Stability and Transition in Shear Flows*. Springer.

Sheard, G., Thompson, M. & Hourigan, K. 2001 A numerical study of bluff ring wake stability. In *Proc. 14th Australasian Fluid Mech. Conf. Dep. Mech. Engng, University of Adelaide*.

Sreenivasan, K. R., Strykowski, P. J. & Olinger, D. J. 1987 Hopf bifurcation, Landau equation, and vortex shedding behind circular cylinders. In *Proc. Forum on Unsteady Flow Separation* (ed. K. Ghia), pp. 1–13. ASME.

Strykowski, P. J. & Sreenivasan, K. R. 1990 On the formation and suppression of vortex 'shedding' at low Reynolds number. *J. Fluid Mech.* **218**, 71–107.

Tannehill, J. C., Anderson, D. A. & Pletcher, R. H. 1997 *Computational Fluid Mechanics and Heat Transfer*, 2nd edn. Taylor & Francis.

Trefethen, L. N., Trefethen, A. E., Reddy, S. C. & Driscoll, T. A. 1993 Hydrodynamics stability without eigenvalues. *Science* **261**, 578–584.

Triantafyllou, G. S. & Karniadakis, G. E. 1990 Computational reducibility of unsteady viscous flows. *Phys. Fluids* A **2**, 653–656.

Williamson, C. H. K. 1988 Defining a universal and continuous Strouhal–Reynolds number relationship for the laminar vortex shedding of a circular cylinder. *Phys. Fluids* **31**, 2742–2744.

Williamson, C. H. K. 1996 Vortex dynamics in the cylinder wake. *Annu. Rev. Fluid Mech.* **28**, 477–539.

Winters, K. H., Cliffe, K. A. & Jackson, C. P. 1986 *The Prediction of Instabilities Using Bifurcation Theory*. Wiley.

Yang, X. & Zebib, A. 1988 Absolute and convective instability of a cylinder wake. *Phys. Fluids* **1**, 689–696.

Ye, T., Mittal, R., Udaykumar, H. S. & Shyy, W. 1999 An accurate Cartesian grid method for viscous incompressible flows with complex immersed boundaries. *J. Comput. Phys.* **156**, 209–240.

Zebib, A. 1987 Stability of viscous flow past a circular cylinder. *J. Engng Maths* **21**, 155–165.

Zielinska, B. J. A., Goujon-Durand, S., Dusek, J. & Wesfreid, J. E. 1997 Strongly nonlinear effect in unstable wakes. *Phys. Rev. Lett.* **79**, 3893–3896.

Zielinska, B. J. A. & Wesfreid, J. E. 1995 On the spatial structure of global modes in wake flows. *Phys. Fluids* **7**, 1418–1424.